Development and testing of a stereo photogrammetry system for multi-axis optical tracking of free-flight models

Georgia E. Warren[1]

The University of New South Wales Canberra at the Australian Defence Force Academy, Campbell, ACT, 2612, Australia

Free-flight testing is an increasingly popular technique in which relatively simple models move unconstrained in a wind tunnel test section without interference effects from a supporting sting. Their motion is usually measured by an onboard inertial measurement unit (IMU) or image tracking using high-speed video footage. Stereo photogrammetry has been used in several studies attempting to measure motion in the horizontal plane. However, systems capable of measuring complex 3-D motion are scarce and there is a high degree of uncertainty in the accuracy of these systems. This work presents the experimental approach used to develop and test a new stereo photogrammetry system for multi-axis optical tracking of free-flight models in hypersonic wind tunnel facilities. Two synchronized high-speed cameras mounted at 45 degrees from the horizontal on either side of a simulated test section were used to record footage of known model translations and rotations simultaneously measured by an onboard IMU. Commercial digital image correlation (DIC) software and custom Python code were then used to obtain accelerations and angular accelerations from displacement-time data and comparison of the two measurement techniques enabled uncertainty analysis of the image tracking results. As a demonstration, this work measures the falling dynamics of a hypersonic vehicle model upon release by a Chebyshev lambda mechanism to which a rapidly retracted platform is attached. Measured accelerations and angular accelerations are compared to onboard IMU measurements and the predicted motion of the model, with maximum differences of 2.21 m/s^2 and 2660 deg/s^2 between the IMU and image tracking results and maximum RMSEs of 0.617 m/s^2 and 404 deg/s^2 between the image tracking results and predicted motion. This new approach may enable accurate measurement of model motion in three dimensions with a clearer understanding of the level of uncertainty in image tracking results than observed in previous literature.

I. Nomenclature

a	=	acceleration, m/s^2
dt	=	time step, s
r	=	radius, m
v	=	velocity, m/s
x	=	displacement, m
U	=	absolute uncertainty
α	=	angular acceleration, deg/s^2
Δ	=	difference between
θ	=	angular displacement, deg

Subscripts

i	=	ith element in a time series
i-1	=	element preceding the ith element in a time series
IMU	=	inertial measurement unit
IT	=	image tracking
max	=	maximum

---

[1] Undergraduate, UNSW Canberra School of Engineering and Technology, AIAA Student Member.

II.   Introduction

Hypersonic flows are characterized by flow speeds of more than five times the speed of sound and feature thin shock layers, strong entropy gradients, and viscous interaction due to their high temperatures and low densities [1]. These flow phenomena pose significant challenges in terms of integrating the airframes and propulsion systems of hypersonic vehicles, mitigating aerodynamic heating, and managing drag [1].

Hypersonic vehicle designs are commonly tested by means of flight testing, ground testing, and numerical simulation [2-4]. Flight testing has the highest fidelity of the three but also carries the most risk, and so its use is often limited to later stages of the design process [2-4]. Numerical simulation and tunnel-based testing are the preferred methods for efficient investigation of design feasibility in the earlier stages of the design process. These methods are often used in conjunction with one another to account for uncertainties in modelling factors and as a way of independently validating the results from each [2-5]. In recent years, tunnel-based testing has proven particularly useful for measuring aerodynamic derivatives [2,6-16], investigating the aerodynamics of different vehicle configurations [5,17-20], and reproducing separation kinematics [3,15,16,18,21] as well as for validation of the associated databases or numerical simulations [4,6,10,12,14,15,17-19,21,22].

Tunnel size and flow duration are key constraints on the utility of wind tunnel facilities [3]. Size constraints often require models and flow conditions to be scaled to simulate realistic flight conditions and the response times of measurement devices must be significantly shorter than the flow duration of the tunnel to measure dynamic behaviour [2,4,5]. In conventional wind tunnel testing, models are generally supported by a sting equipped with a force balance for measurement of aerodynamic forces and moments [2,4,5,18]. This sting generally increases drag and introduces error by causing disturbances in the wake of the supported model [2,5,18,23]. Furthermore, rapid force measurement or advanced deconvolution techniques are often required for force balances to acquire meaningful results in supersonic and hypersonic flows on the order of a few hundred milliseconds [2,4,5,18].

Free-flight testing is an increasingly popular solution to the complications associated with measuring dynamic behaviour in hypersonic wind tunnel facilities. In free-flight testing, an unsupported model is released in the test section of the tunnel just prior to the flow being initiated over the model which then moves unconstrained for the duration of the flow [2,4,5,18]. The two most common measurement techniques used to track the motion of a free-flight model are the use of an onboard inertial measurement unit (IMU) and image tracking using high-speed cameras [2,5,18].

Several single-camera imaging and schlieren interferometry systems have been successfully used to measure lift, drag, and pitching moment coefficients in the longitudinal plane parallel to the field of view of the camera [2,4,6,10,11,14,15,18,21,24,25]. The key limitation of these systems, however, is their inability to accurately measure motion in planes perpendicular to the field of view of the camera, i.e., sideslip, roll, and yaw [2,4,6,11,18,21,24]. One solution is to use multiple cameras to measure motion outside of the longitudinal plane by employing stereo photogrammetry which estimates 3D marker coordinates based on measurements made in corresponding camera views. Attempts have been made in recent years to develop stereo photogrammetry systems to track model motion in three dimensions [16,17,26-30], however, little work has been done to characterise the uncertainty in measurements taken by these systems and indeed to demonstrate their successful use in free-flight experiments.

A.   Aim and Significance

The aim of this work is to develop and test a new stereo photogrammetry system for multi-axis optical tracking of free-flight models in hypersonic wind tunnel facilities. This work also seeks to characterise the uncertainty in measurements taken with this system and to demonstrate its successful use in tracking the motion of a hypersonic vehicle model upon separation from a wind tunnel release mechanism to validate simultaneous IMU measurements.

To achieve this aim, two synchronized high-speed cameras mounted at 45 degrees from the horizontal on either side of a simulated test section were used to record footage of known model translations and rotations simultaneously measured by an onboard IMU. Commercial digital image correlation (DIC) software and custom Python code were then used to obtain accelerations and angular velocities from displacement-time data and comparison of the two measurement techniques enabled uncertainty analysis of the image tracking results. As a demonstration, the falling dynamics of a hypersonic vehicle model were then measured upon release by a Chebyshev lambda mechanism to which a rapidly retracted platform was attached. The accelerations and angular velocities measured by the stereo photogrammetry system were compared to the onboard IMU measurements.

Development of the system was based on the work of Zhang et al. [30] and Moran et al. [31] and involved careful consideration of the numerous possible sources of error cited in the literature, including depth of field, exposure, marker positioning, lighting and contrast, optical distortion, motion-related blurring, pixelation, calibration errors, optical system misalignment, and noise amplification due to differentiation of displacement-time data in postprocessing [14,16-18,26-30]. Addressing both the inability of single-camera systems to accurately measure motion outside of the longitudinal plane, and the high degree of uncertainty in the accuracy of current single- and multi-camera systems, this system may be used to facilitate more rigorous investigation of 3-D flight dynamics in hypersonic wind tunnel facilities.

III.   Literature Review

A.   Motivation and Uses

The free-flight technique originated as a means of overcoming sting interference effects and the severe distortion of hypersonic flows around sting mounted models [23]. One key study by the Naval Ship Research and Development Center in 1971 found base pressure measurements to differ by up to 70% between sting-mounted and free-flight models due to flow distortion around the sting [23].

Furthermore, free-flight testing sought to overcome the large signal-to-noise ratios obtained by sting-mounted force balances lacking the temporal response for measurement of dynamic behaviour in millisecond-order flow durations [10]. While advanced deconvolution techniques have been used in a few studies to obtain results within 1% [7] and 17% [32] of their theoretical values from sting-based force balances, these techniques still failed to account for sting interference effects and were found to be costly, computationally expensive, and relatively complicated, particularly in terms of accounting for the effects of tunnel vibration [2,4,5,9,18].

Instead, free-flight testing has been successfully employed to investigate the feasibility of hypersonic vehicle designs by means of aerodynamic testing [5,17,19,20,31] and the measurement of forces, moments, aerodynamic coefficients, vehicle stability coefficients, dynamic stability derivatives [2,7-16], and pressure [33]. The technique has also been used to investigate the aerodynamics of cones, cubes, and spherical bodies as well as separation kinematics [3,15,18,21], the behaviour of proximal bodies [25], fluid-thermal-structural interaction [34], and aerothermal loading [35-37].

B. Early Contributions

The development of onboard instrumentation and both single- and multi-camera systems for model position and attitude measurement is well-documented in the literature and several studies advocate for the combined use of onboard instrumentation and imaging systems as a means of independently validating the results from each [2-6,12,13,15-20,22,25,31].

Initially, single-camera systems began as passive electro-optical tracking systems where laser backlighting was used for the projection of model shadows onto photodiode arrays, enabling measurement of aerodynamic forces and moments exclusively in the longitudinal plane [11,24]. This was followed by the use of high-speed cameras to record the projection of model shadows onto opaque screens [38] and the use of schlieren systems for simultaneous flow visualisation and measurement of lift, drag, and moment coefficients in the longitudinal plane [14,15,21,25]. Studies employing these techniques tended to either deliberately constrain motion to the longitudinal plane or assume sideslip, roll, and yaw to be negligible.

Schlieren systems were instrumental in the development of onboard instrumentation as pressure, force, moment, and heat flux measurements could be validated against schlieren images to verify the accuracy of the results obtained [12,13,19,20]. Schlieren and other image-based techniques quickly became a supplement to the use of onboard instrumentation and comparison with computational modelling became commonplace. Several studies have used schlieren imaging and onboard instrumentation to measure aerodynamic coefficients in the longitudinal plane, generally with good agreement both between the two methods and often also with numerical simulations or numerically derived databases [2-4,6,10,18,22].

Recent studies have also used a single high-speed camera to record video footage of model motion rather than schlieren imaging. Hyslop et al. [5] combined the use of onboard instrumentation, schlieren, and direct imaging and compared the results from each as a means of independent validation. Challenges identified in the use of onboard instrumentation and both single-camera and schlieren systems include 1) limited field of view and poor lighting [10,15], 2) considerable noise introduced by differentiation of displacement-time data [5,6,14], 3) accumulation of measurement error with longer test durations [18], 4) calibration errors and misalignments in the imaging system [11], 5) uncertainty due to pixelation, sensor noise, optical distortion, motion-related blurring, tunnel vibration, and flow unsteadiness [14,21], 6) insufficient insulation of instrumentation from ionisation in the flow [15], and 7) the external presence of onboard instrumentation affecting the lift of secondary bodies [25]. In all of these studies, measurements taken by the imaging system were limited to lift, drag, and pitching in the longitudinal plane.

C. Current State of Knowledge

A proposed solution to the inability of single-camera systems to reliably measure motion outside of the longitudinal plane (i.e., sideslip, roll, and yaw) came with the early development of multi-camera systems for position and orientation tracking of free-flight models. In 1993, Meyn and Bennett [39] successfully used a two-camera system, stereo ranging, and epipolar geometry to track the vortices produced by the leading-edge extensions of a full-scale F/A-18. This was then followed by the development of further multi-camera systems for 3-D position and attitude measurement of free-flight models. Shortis and Snow [26] used systems with two and three synchronised CCD cameras to compute model position using centroid computation, collinearity equations, and least squares estimation, while Gui et al. [27] used two cameras, a correlation-based algorithm, and geometrical relations between markers to determine the six motion variables of interest. In the former case, the cameras were calibrated by imaging both a straight line and targeted test field to establish a coordinate system by which displacements could be measured [26]. The first system also used known marker locations to determine the pose of the cameras relative to a specified tunnel coordinate system [26].

Both systems used the 2-D positions of markers in corresponding camera views and the known view angles of the cameras to reconstruct the markers' 3-D coordinates by projecting the two views onto a common measurement plane [26,27]. The first system was believed to show promise in terms of its accuracy and reliability, however more advanced algorithms and technology were deemed necessary to improve measurement efficiency and overcome the limitations of the analogue recording system used [26]. The second system was also believed to show promise in determining model coordinates, however, was only tested on synthetic pairs of images from simulated model motion and was limited by poor contrast and obscuration of markers in these images particularly in roll to which the highest errors were attributed likely due to the smaller observed dimension in the radial direction as both cameras viewed the model from the same sidewall [27]. In both cases, camera positioning, lighting, and marker positioning were recognised as being particularly important for successful measurement [26,27].

More recent systems have been used by Schairer et al. [28] in a supersonic wind tunnel to measure the position and attitude of a slender body supported by a flexible sting, and by Seltner et al. [16] to measure the aerodynamic coefficients of a free-flying cube. Both systems employed stereo photogrammetry and the use of a rectangular calibration plate [28] or other calibration object [16] imaged at various angles to map coordinates in 3-D space to points in each 2-D camera view by means of triangulation and to

determine the intrinsic (e.g., focal length) and extrinsic (e.g., position and orientation) camera parameters. Both also used static reference markers (e.g., on the tunnel walls) to define a coordinate system by which displacements could be measured, utilising ellipse-fitting and marker-based least-squares tracking algorithms [16,28]. The system used by Schairer et al. [28] experienced significant issues with lighting and marker visibility due to the contrast between the model and markers as well as large uncertainties in roll like those faced by Gui et al. [27]. These uncertainties were attributed to close positioning of markers to the roll axis (and likely also the smaller perceived dimension in the roll direction due to both cameras being mounted in the same sidewall). The photogrammetry software used also required manual point-and-click identification of markers in thousands of frames, significantly reducing measurement efficiency [28]. The system used by Seltner et al. [16], on the other hand, suffered from an unfavourable signal-to-noise ratio as a result of noise amplification caused by differentiation in postprocessing, similar to other systems [5,6,14]. Roll and yaw were also neglected to reduce analysis to three degrees of freedom and thereby reduce complexity [16].

Hyslop et al. [17] then took an alternative approach, moving away from stereo photogrammetry and instead using one high-speed camera to track motion in the longitudinal plane and one to track the yaw axis. Again, a calibration grid was used to determine camera parameters and correct for optical distortions as with other multi-camera systems [16,28] and the known location of the model's centre of gravity (COG) and trigonometric relations were used to determine its angle of attack [17]. Displacement-time and velocity-time data were smoothed between differentiations to limit noise growth in computing accelerations and these accelerations agreed well with onboard IMU results in the longitudinal plane [17]. The utility of the camera used to horizontal plane, however, was limited to confirming the model exhibited minimal yaw as the increasing distance between the yaw plane and camera as the model fell complicated accurate measurement of roll and yaw [17]. Moran et al. [31] then attempted to perform stereo image tracking with two cameras on either side of the tunnel mounted at 45 degrees to the horizontal and one camera above, however the image tracking results were omitted.

In 2021, a stereo photogrammetry system for position and attitude measurement of free-flight models was developed by Zhang et al. [30] and featured a robust cross calibration method involving three cameras and various calibration targets to account for tunnel vibration. A cone model was successfully tracked undergoing translation along the x-axis, pitch, and yaw independently all facilitated by a supporting mechanism, translation and pitch outside a hypersonic wind tunnel followed by pitch and yaw inside a hypersonic wind tunnel [30]. Measured trends were observed to be reasonable and correct, however, no uncertainty analysis was included in the discussion and tunnel vibration was still hypothesised to have influenced the accuracy of the results [30]. The system was then used to measure motion in free-flight, with the results indicating unexplainable trends in roll and yaw [30]. Belief in the potential measurement capability of the system was therefore based on the continuity and smoothness of the curves obtained with no further discussion of measurement accuracy [30].

D. Novelty of Contribution

Both single- and multi-camera systems used for model position and attitude measurement are susceptible to numerous sources of error including those introduced by the equipment [10,14,15,21], incorrect or suboptimal use or calibration of the equipment [11,15,17,27,28], and amplification of noise in postprocessing [5,6,14]. These sources of error can be challenging to quantify particularly when amplified by double differentiation of displacement-time data to obtain accelerations.

The inability of single-camera systems to measure motion outside of the longitudinal plane is addressed by incorporating multiple cameras and using stereo photogrammetry to measure motion in 3-D. Many sources also advocate for the additional use of onboard instrumentation as a means of independently validating image tracking results [2-6,12,13,15-20,22,25,31]. Key considerations for multi-camera systems in particularly in terms of minimising experimental error are the positioning of both cameras and model markers and the visibility of markers in both camera views in terms of lighting and contrast [16,26-28]. Measurement efficiency is also a key consideration [26,28].

There is a distinct lack of understanding of the accuracy of multi-camera systems in the literature and many studies have limited their utility for measurement outside of the longitudinal plane to confirmation of negligible sideslip, roll, and yaw, rather than precise measurement of these quantities, particularly roll [16,17,27,28]. This work describes the approach taken to develop and test a stereo photogrammetry system capable of accurately measuring all six motion variables and the attempts made to characterise the uncertainty in measurements taken by the system. The broader aim of developing this system and quantifying its uncertainty is to expand the capability of tunnel-based testing to assess the feasibility and aid in the optimisation of hypersonic vehicle designs.

Nearing the conclusion of this study, Lock et al. [40] published a study into a new method of six degree-of-freedom aerodynamic measurements using two unsynchronised and arbitrarily positioned cameras, one in an existing z-type schlieren system. The locations of detected markers in each camera view are related to model position and attitude in a local coordinate system using calibrated camera models which allows these views to be treated individually [40]. A kinematic process model based on Bayesian state estimation is used to compute aerodynamic measurements based on marker coordinates in the local coordinate system [40]. This new method aims to overcome the challenge of camera positioning constraints in hypersonic wind tunnel facilities and the unfavourable signal-to-noise ratios commonly observed in optical aerodynamic measurements [40]. The aerodynamics of a free-flying cube were measured and compared to CFD simulations with strong agreement between the two result sets and effective noise reduction compared to those commonly observed in similar applications [40].

Experimental sources of error cited to have potentially impacted tracking accuracy included tunnel vibration, obvious angular tracking errors when only one face of the cube was visible to each camera, and the inherent difficulty of Kalman filters to detect large and fast state changes without accentuating measurement noise, as well as inevitable errors arising from camera calibration and marker detection due to lighting, marker positioning, and camera resolution [40]. While this work shows promise for accurate tracking of complex 3-D motion, it has yet to be tested on a representative hypersonic vehicle configuration unlike the work detailed herein. It is likely both methods may be useful in expanding optical measurement capability in free-flight experiments.

4

IV.   Methodology

A. Vehicle Model and Onboard Inertial Measurement Unit

The vehicle geometry selected for use was the Air Force Research Laboratory's Initial Concept 3.X which features an axisymmetric cylindrical body with cruciform diamond airfoil fins and a nose section in the shape of a power law curve [34]. The model (Fig. 1) was scaled to a length of 254 mm and a maximum body diameter of 25.7 mm or 1/14th of the intended dimensions for the full-scale model as this size ensures complete visibility in the test section of the TUSQ hypersonic wind tunnel facility where the model is likely to be tested. Modifications to the geometry included the incorporation of a cylindrical sled used to house an IMU printed circuit board (PCB) and battery as well as a modular design separating body and nose to facilitate ease of their replacement, particularly in the case of damage to the fins. Countersunk fasteners at either end of the body were used to secure the components together and holes were extruded in the nose and base of the model to enable its attachment to a rotating mechanism.
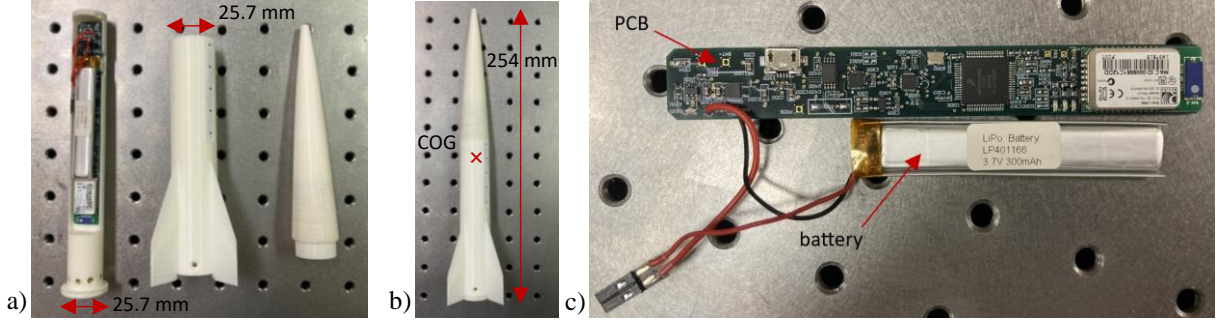
Fig. 1   Images of: a) model components, b) assembled model, and c) onboard IMU.

The IMU PCB (Fig. 1) was secured to the sled by a temporary adhesive and was aligned to take measurements about the model's ideal COG. It was powered by a single-cell lithium-ion polymer (LiPo) battery also housed within the sled and secured by a temporary adhesive. The instrument was connected via Bluetooth to a laptop on which a terminal emulator communicated with the instrument and facilitated both calibration and data collection and display. The multiaxial combination of a three-axis accelerometer and a three-axis gyroscope on a single-chip device in the printed circuit assembly enabled collection of acceleration and angular velocity data in the x, y, and z directions, triggered by measurement of an acceleration or angular velocity above 0.1 g or 30 deg/s in magnitude respectively. In addition to the accelerometer and gyroscope, the IMU also consisted of non-volatile memory, a Bluetooth radio module, and a microcontroller. These components were integrated on a $\approx 114 \times 12$ mm PCB by Hyslop et al. [5] who successfully used this device to collect accurate acceleration and angular velocity data in previous work. The full-scale ranges, data output rates, and nonlinearities were ± 16 g, 4 kHz, and 0.5% respectively for the accelerometer and ± 2000 deg/s, 8 kHz, and 0.1% respectively for the gyroscope [5].

Arduino code was used to program the IMU, notably to specify the sample time and delay between samples (to artificially slow the sampling rate) as well as to specify the axis and magnitude of the trigger. Triggers of 0.1 g and 30 degrees per second were used for the translation and rotation experiments respectively and a trigger of 0.1 g was used for model release. The required triggers for translation were determined using preliminary image tracking results from translation of a rectangular array of markers, while the required triggers for rotation and model release were determined using the predicted acceleration of the servomotors and predicted acceleration in sustained freefall respectively.

Initially, strips of black circle markers 2 mm in diameter and 12 mm apart were temporarily adhered to the model along the longitudinal axis at regular intervals circumferentially (Fig. 2) to allow selection of between four and nine appropriate markers [26,27] for mono or stereo applications. In the rotation and model release experiments, however, only the five markers on the top of the model were tracked as only these markers remained in full view of both cameras. All other markers were removed for these experiments to avoid misdetection of the desired markers. Temporarily adhering markers to the model in strips provided flexibility to easily add or remove markers while maintaining regular spacing between them along the longitudinal axis. Circle markers were chosen over the other possible markers detected by the DIC software, Mercury RT®, as their detection was observed to be the least affected by overexposure and distortion.

Fig. 2   Images of the markers on the axisymmetric body of the model.

B. Camera Setup

High-speed video footage was captured by two Chronos 2.1-HD High Speed Cameras equipped with Nikon 35 mm lenses. The cameras were mounted at the same horizontal and vertical distances from the benchtop test area, each at an angle of 45 degrees to the horizontal (Fig. 3) to comply with the camera positioning constraints of the TUSQ hypersonic wind tunnel facility. They were configured to view the same portion of the test area with a resolution of 1920x1080 and various frame rates depending on the experiments being conducted. These included frame rates of 100 fps for translation, 200 fps for pitch and roll, 500 fps for yaw, and 1000 fps for model release. The cameras were connected by BNC cables to an arbitrary function generator used to facilitate synchronous triggering by means of a manually triggered pulse function. The frequency of the function specified the frame rate of the cameras while the number of cycles specified the number of frames, and the duty cycle specified the exposure.
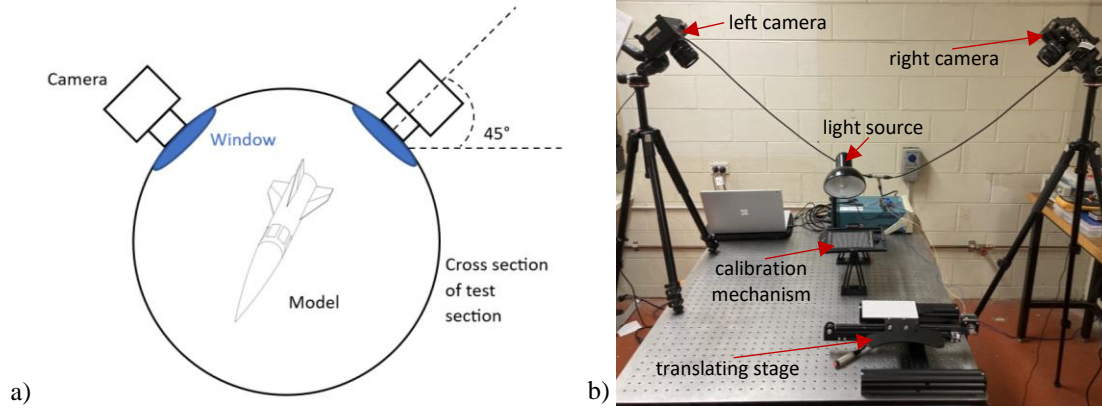
Fig. 3   a) Schematic illustration of the camera positioning constraints in TUSQ and b) photo of the experimental setup.

C. Translating Stage and Rotating Mechanism

Known translations and rotations of the model were measured by both the onboard IMU and photogrammetry system and compared to facilitate error analysis and to repeatedly demonstrate reliable and accurate measurement of motion in the longitudinal and horizontal planes. The aim of the error analysis was to characterise error in the onboard IMU and photogrammetry system results by comparing them to the known motion of the model. Three different distances and angles were selected for translation along and rotation about each axis with three trials conducted for each distance and angle. The distances and angles selected are shown in Table 1.

Table 1   Test matrix

Variable	Start	Stop	Points	Trials
Distance Translated (cm)				
X	3	5	3	3
Y	1	3	3	3
Z	2	4	3	3
Total (3×3×3)				**27**
Angle Rotated (°)				
X (Roll)	10	30	3	3
Y (Pitch)	5	15	3	3
Z (Yaw)	5	15	3	3
Total (3×3×3)				**27**
Model Release				
Total (1×9)				**9**
Total				**63**

Translation of the model was facilitated by a translating stage to which a cradle was fastened to hold the model. The stage consisted of a flat plate attached to a belt which was driven by a stepper motor connected to an Adafruit Motor Shield v2.3 on an Arduino MEGA 2560 board and powered by a Tektronix PWS2323 DC Power Supply outputting 5 V and 3 A. Translation in the x, y, or z directions was facilitated by appropriate orientation of the stage relative to the cameras (Fig. 4). A circuit containing two LEDs was also connected to the Arduino MEGA 2560 board which in turn was connected to a laptop by a USB cable. The LEDs were taped to the stage in view of both of the cameras and used to indicate when the stage had started and stopped moving. The stepper motor was programmed to translate the stage a specified distance and then pause for 100 ms before returning to its initial position with the LEDs switched on only while the stage was translating forward and for a specified delay once the stage had returned to its initial position. Of the four different motor pickups available for use (single coil, double coil, interleave, and microsteps), the interleave pickup was used as preliminary image tracking results from the translation of a rectangular array of markers indicated this pickup produced the least vibration.
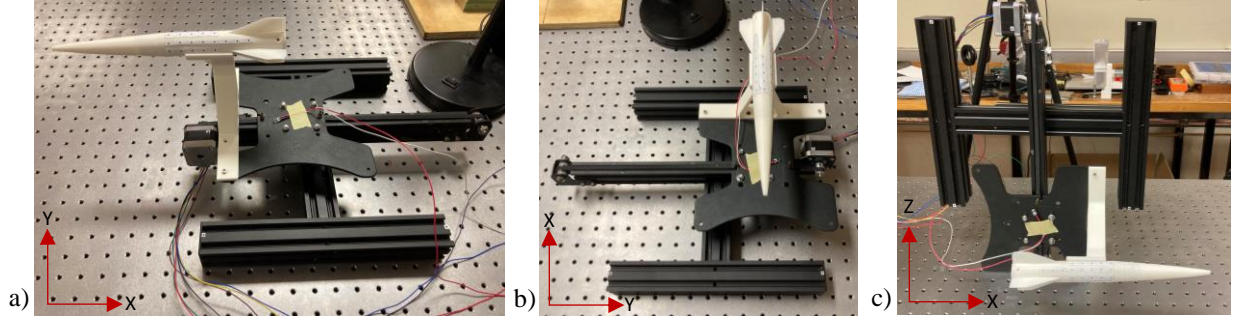
6

Fig. 4   Images of the translating stage for translation along the: a) x-axis, b) y-axis, and c) z-axis.

A modified version of the rotating mechanism currently used by the UNSW Hypersonic Vehicles Group for camera calibration was designed and fabricated with attachments to secure the model to the mechanism. This mechanism was able to rotate either a calibration grid or the model about two different axes either independently or simultaneously by means of two servomotors attached to the same Adafruit Motor Shield and Arduino MEGA 2560 board as the translating stage. In both cases, the mechanism was fastened to the benchtop in complete view of both cameras in the area of interest in which experiments took place, and the grid or model rotated about fixed axes.

Calibration was performed before each round of experiments (translation, rotation, and model release) and produced a calculated reprojection error of 0.1 px. In the case of camera calibration, the rotating mechanism was fitted with a specific rectangular array of markers known as an enhanced circle grid (Fig. 5) and was used to position the grid at 81 different combinations of angles spanning all possible combinations of -20, -15, -10, -5, 0, 5, 10, 15, and 20 degrees about both axes. The mechanism was programmed to move to a new position based on user commands from the laptop to which the Arduino board was connected. One image of the grid at each position was captured by each camera and the 162 images were uploaded to Mercury RT® for mapping of the marker positions in 3-D space to points in each of the 2-D camera views. This enabled the software to establish a coordinate system by which displacements could be measured and to calculate an overall reprojection error indicating the accuracy of the cameras in detecting the markers.

In the case of model rotation, the grid was removed, attachments were inserted into the nose and base of the model, and the model attachments were fastened to the mechanism. Like the translating stage, the mechanism facilitated rotation about the x, y, or z axes depending on its orientation relative to the cameras (Fig. 5) and the attachments were designed to ensure the model would rotate about its ideal COG. LEDs were taped to the rotating mechanism in view of both cameras and used to indicate when the mechanism had started and stopped moving. The mechanism was programmed to move to a specified angle about one of its two axes with the LED switched on for the entire movement.
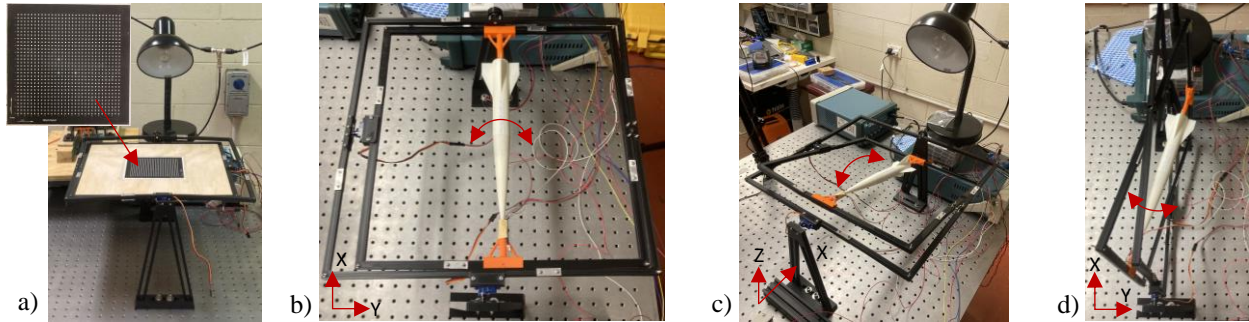

Fig. 5   Images of the rotating mechanism for: a) calibration and rotation about the b) x-axis, c) y-axis, and d) z-axis.

D. Release Mechanism

Release of the model by a benchtop version of the wind tunnel release mechanism currently used in TUSQ [40,41] was then tracked to demonstrate the utility of the stereo photogrammetry system in free-flight experiments. The Chebyshev lambda mechanism was fabricated from steel sheet and plate parts assembled on a plywood board (Fig. 6) and achieves reliable model release by moving a rapidly retracted platform vertically downward without disturbing or imparting rotation to the model during separation. The mechanism is actuated by means of two solenoids which hold the mechanism in its initial position until a button is pressed which energises the solenoids to initiate release. The solenoids are powered by a GW Instek GPS-1850D DC power supply delivering 12 V and 1 mA.
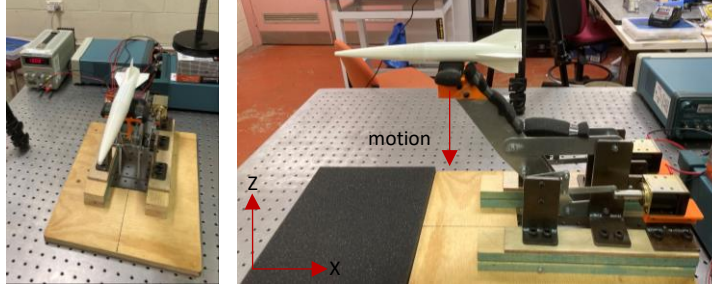
Fig. 6   Images of the release mechanism.

E. Photogrammetry and Postprocessing

A commercial DIC software, Mercury RT®, was used to process the calibration images and establish a coordinate system by which displacements could be measured, as well as to detect markers in corresponding camera views, determine marker coordinates by means of centroid computation and triangulation, and calculate the displacements of the markers in time. For the image tracking results, custom Python code was used to calculate and filter velocities and accelerations of the markers and angular displacements, velocities, and accelerations of the model as an average of the five markers. For the IMU results, the code was used to filter marker accelerations and angular velocities obtained and calculate and filter angular accelerations. Both the IMU and image tracking results were filtered using a low-pass Butterworth filter with cutoff frequencies based on the spectral plots of each time series. Results from each technique were compared with the predicted motion of the model. The root mean squared error (RMSE) of both techniques was evaluated for each experiment and the two techniques were compared by calculating the differences between them and performing linear regression. A diagrammatic representation of the postprocessing code is shown in Fig. 1 of Appendix A.

V.   Results and Discussion

The standard process for propagation of uncertainties in velocities, accelerations, and angular displacements, velocities, and accelerations calculated from displacement-time data is demonstrated in Appendix B. As shown, differentiating over relatively short timesteps between 1 and 10 milliseconds results in significant propagation of uncertainty resulting in the tabulated values presented in Table 1 of Appendix B. Instead of relying on the standard process, which would see uncertainties of up to 400 m/s^2 in the measurement of gravitational acceleration, this section seeks to quantify uncertainty in terms of the maximum RMSE of both the image tracking and IMU results when compared to the programmed or predicted motion of the model. Reliability is then quantified in terms of the range of maximum RMSEs in each group of nine trials. Error bars have hence been omitted in the plots of this section as the uncertainties calculated in Appendix B are not considered reflective of the true measurement capability of the IMU and stereo photogrammetry system.

The maximum difference in acceleration or angular acceleration between measurement techniques (Δa_{max} or $\Delta \alpha_{max}$) across each group of nine trials provides a good indication of the maximum extent to which the two measurement techniques differ in measurement of the same quantity. Maximum RMSE between the image tracking and IMU results respectively and the programmed or predicted motion of the model for each group of nine trials then provides a good indication of the measurement uncertainty of each technique in each experiment. RMSE is preferred over other types of error in this work because residuals are squared to give more weight to larger errors and therefore more appropriately account for outliers in determining how close the measured results are to the programmed or predicted values on average. All metrics are given in both absolute and percentage terms to provide context as to how large each difference or uncertainty is relative to the maximum measured values.

A. Model Translation

Three trials of three different distances were recorded along each of the three axes of motion, totalling 27 experiments. Displacement, velocity, and acceleration data from stereo image tracking and acceleration data from the onboard IMU are shown for all 27 experiments. These results are then compared to the motion of the stage used to translate the model, which was programmed to translate a specified distance, stop for 100 ms, then return the model to its starting position. Differences between the stereo image tracking and onboard IMU acceleration as well as and the RMSE between these data and the programmed motion are shown in Table 2.

Table 2   Maximum differences between measurement techniques and maximum RMSE for each technique

Axis	Δa_{max} (m/s^2)	a_{max} (m/s^2)	%Δa_{max}[1] (%)	RMSE$_{max,IT}$ (m/s^2)	%RMSE$_{max,IT}$[2] (%)	RMSE$_{max,IMU}$ (m/s^2)	%RMSE$_{max,IMU}$[3] (%)
X	2.80	2.16	129	0.117	13.6	0.686	37.0
Y	1.07	0.588	181	0.125	25.5	0.238	29.3
Z	1.16	0.681	171	0.117	19.9	0.296	43.5

[1]Δa_{max} divided by the maximum acceleration (either $a_{max,IT}$ or $a_{max,IMU}$) measured in the trial containing Δa_{max}.
[2]RMSE$_{max,IT}$ divided by $a_{max,IT}$ in the trial containing RMSE$_{max,IT}$.
[3]RMSE$_{max,IMU}$ divided by $a_{max,IMU}$ in the trial containing RMSE$_{max,IMU}$.

Figures 7, 8, and 9 show both the stereo image tracking and onboard IMU results from a typical trial overlaid on a plot of the programmed motion of the model and the stereo image tracking results from all nine trials along the x, y, and z axes respectively overlaid on plots of the programmed motion of the model. Larger versions of these figures are shown in Appendix C. Some agreement can be observed between the stereo image tracking results and the IMU results, however, there is a considerable level of noise in the IMU results, resulting in measurements up to 1 m/s² for zero acceleration. This noise is likely to have caused the relatively large percentage differences between the two techniques and indeed the larger maximum RMSE of the IMU results (0.686 m/s²) compared to the image tracking results (0.125 m/s²). Relatively good agreement can be observed in image tracking results across the three trials for each angular displacement and between these results and the programmed motion of the model, with RMSE remaining below 0.125 m/s² or 25.5% for all trials.
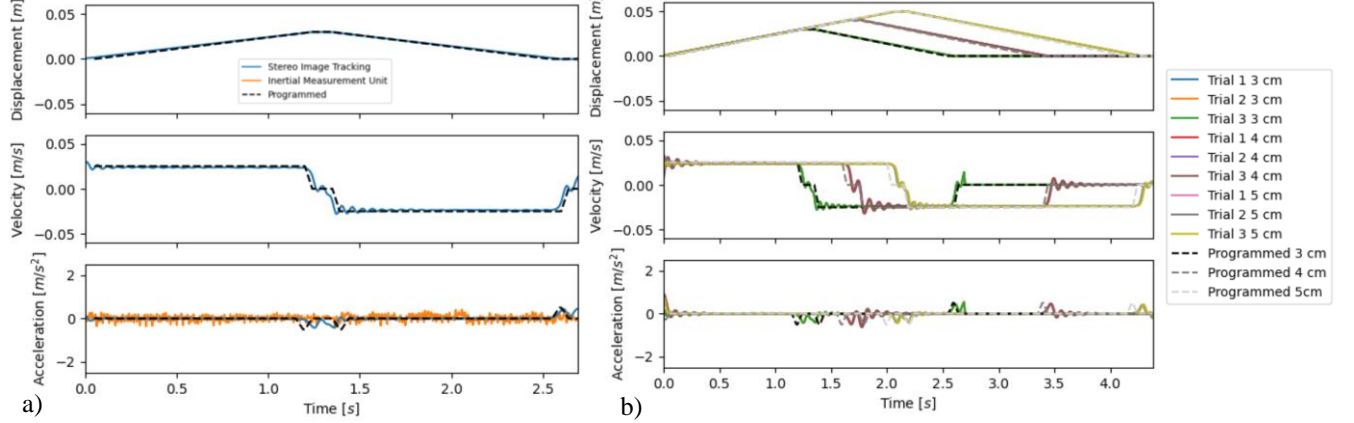
Fig. 7 a) Image tracking and IMU results overlaid on predicted motion for a typical trial and b) image tracking results overlaid on programmed motion for all trials of translation along the x-axis.
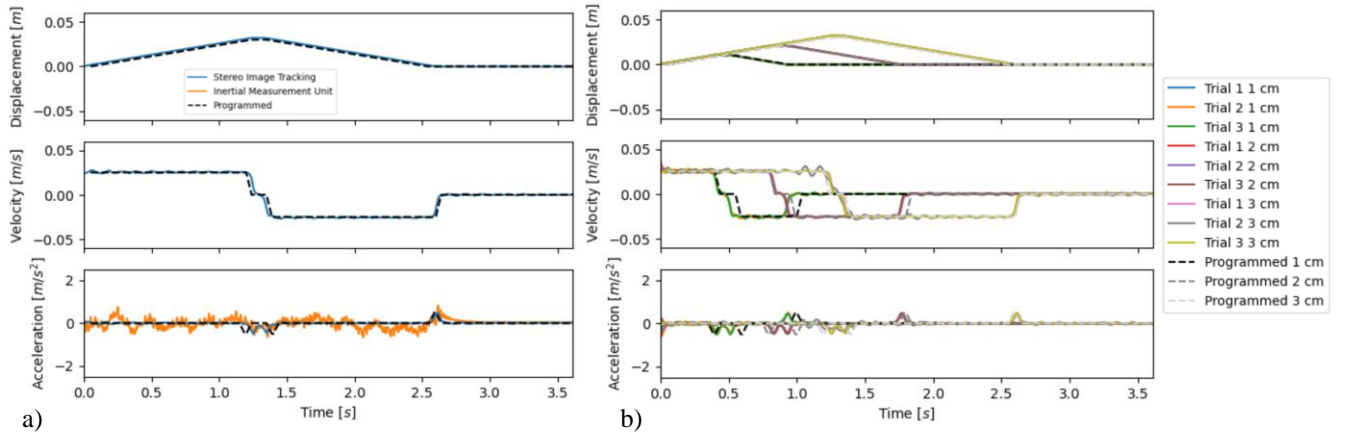
Fig. 8 a) Image tracking and IMU results overlaid on predicted motion for a typical trial and b) image tracking results overlaid on programmed motion for all trials of translation along the y-axis.
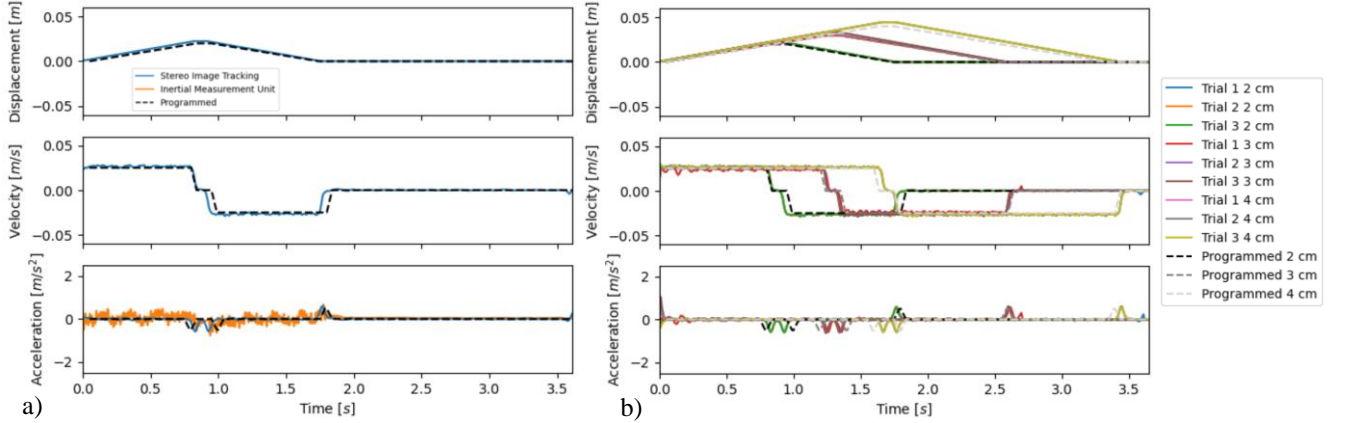
Fig. 9 a) Image tracking and IMU results overlaid on predicted motion for a typical trial and b) image tracking results overlaid on programmed motion for all trials of translation along the z-axis.

Boxplots of the maximum differences between the two measurement techniques as well as the RMSE between each measurement technique and the programmed motion of the model for each of the nine trials along the x, y, and z axes are presented in Figures 10, 11, and 12 respectively. The ranges of the boxplots are tabulated in Table 3. There is a relatively high degree of variability in the maximum difference between the two techniques and the maximum RMSE of the IMU results, with ranges of 2.21 m/s^2 and 0.557 m/s^2 respectively, compared to the maximum RMSE of the image tracking results, with a range of 0.0495 m/s^2. This is likely also due to the noise present in the IMU results and suggests more reliable measurement of translation by the stereo photogrammetry system in these experiments.

Table 3   Ranges of maximum differences between measurement techniques and maximum RMSE for each technique

Axis	Range of Δa_{max} (m/s^2)	Range of %Δa_{max} (%)	Range of RMSE$_{max,IT}$ (m/s^2)	Range of %RMSE$_{max,IT}$ (%)	Range of RMSE$_{max,IMU}$ (m/s^2)	Range of %RMSE$_{max,IMU}$ (%)
X	2.21	30.0	0.0272	9.86	0.557	22.3
Y	0.406	97.8	0.0495	9.86	0.0916	28.0
Z	0.529	65.9	0.0329	10.5	0.159	32.1
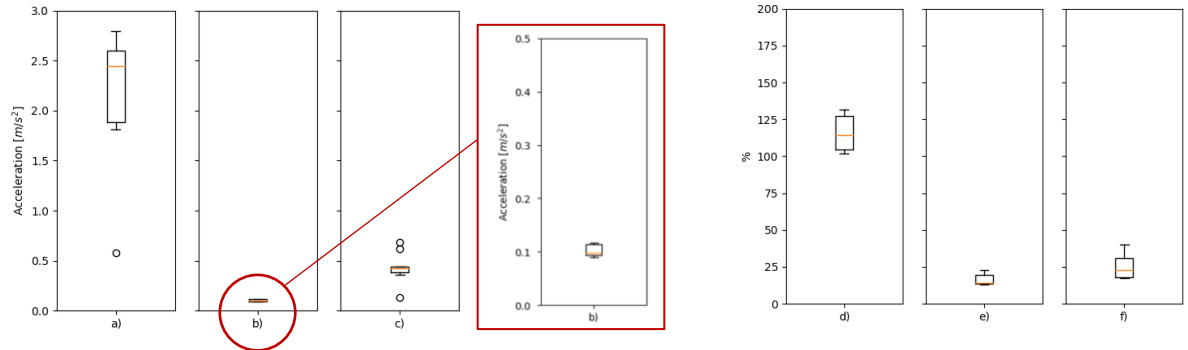
Fig. 10 Boxplots of: a) Δa$_{max}$, b) RMSE$_{max,IT}$, c) RMSE$_{max,IMU}$, d) %Δa$_{max}$, e) %RMSE$_{max,IT}$ and e) %RMSE$_{max,IMU}$ for x-axis.
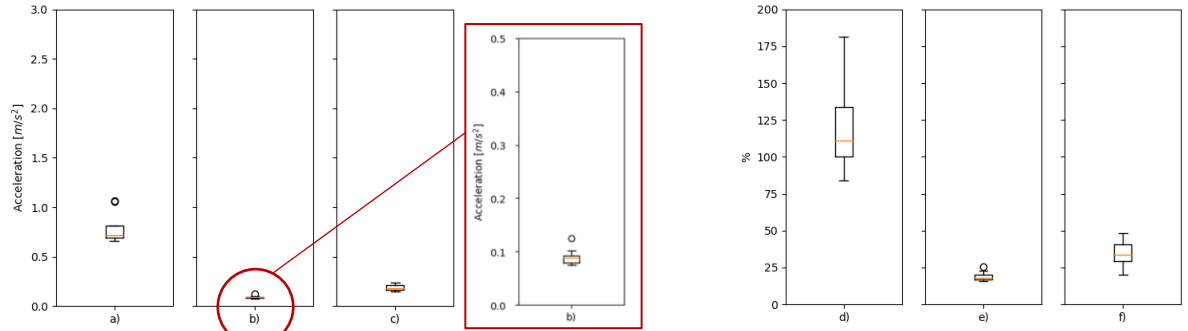
Fig. 11 Boxplots of: a) Δa$_{max}$, b) RMSE$_{max,IT}$, c) RMSE$_{max,IMU}$, d) %Δa$_{max}$, e) %RMSE$_{max,IT}$ and e) %RMSE$_{max,IMU}$ for y-axis.
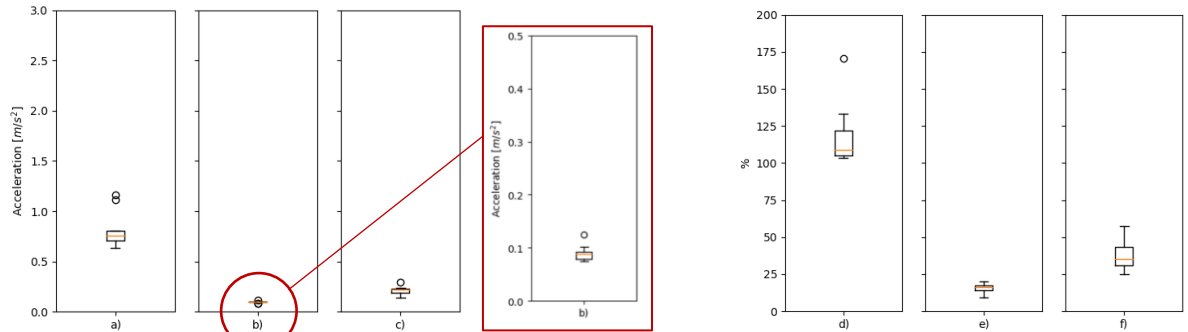
Fig. 12 Boxplots of: a) Δa$_{max}$, b) RMSE$_{max,IT}$, c) RMSE$_{max,IMU}$, d) %Δa$_{max}$, e) %RMSE$_{max,IT}$ and e) %RMSE$_{max,IMU}$ for z-axis.

B. Model Rotation

Three trials of three different distances were recorded about each of the three axes of motion, totalling 27 experiments. Angular displacement, angular velocity, and angular acceleration data from stereo image tracking and angular velocity and angular

acceleration data from the onboard IMU are shown for all 27 experiments. These results are then compared to the programmed motion of the mechanism used to rotate the model. The rotating mechanism was programmed to translate the model to specified angle and then stop. Differences between the stereo image tracking and onboard IMU acceleration as well as and the RMSE between these data and the programmed motion are shown in Table 4.

Table 4   Maximum differences between measurement techniques and maximum RMSE for each technique

Axis	$\Delta\alpha_{max}$ (deg/s^2)	α_{max} (deg/s^2)	$\%\Delta\alpha_{max}$[1] (%)	RMSE$_{max,IT}$ (deg/s^2)	$\%$RMSE$_{max,IT}$[2] (%)	RMSE$_{max,IMU}$ (deg/s^2)	$\%$RMSE$_{max,IMU}$[3] (%)
X (Roll)	2400	2380	101	278	12.7	289	50.9
Y (Pitch)	2660	1670	160	400	24.0	786	71.4
Z (Yaw)	1450	1080	135	404	37.6	644	91.1

[1]$\Delta\alpha_{max}$ divided by the maximum acceleration (either $\alpha_{max,IT}$ or $\alpha_{max,IMU}$) measured in the trial containing Δ_{max}.
[2]RMSE$_{max,IT}$ divided by $\alpha_{max,IT}$ in the trial containing RMSE$_{max,IT}$.
[3]RMSE$_{max,IMU}$ divided by $\alpha_{max,IMU}$ in the trial containing RMSE$_{max,IMU}$.

Figures 13, 14, and 15 show both the stereo image tracking and onboard IMU results from a typical trial overlaid on a plot of the programmed motion of the model and the stereo image tracking results from all nine trials about the x, y, and z axes respectively overlaid on plots of the programmed motion of the model. Larger versions of these figures are shown in Appendix C. Relatively poor agreement within 2660 deg/s^2 can be observed between the stereo image tracking results and the IMU results, likely due to issues with the IMU as the maximum RMSE of the IMU results (786 deg/s^2) was nearly double that of the image tracking results (404 deg/s^2). Moderate agreement can be observed in the image tracking results across the three trials for each angular displacement and indeed between these results and the programmed motion of the model, with RMSE remaining below 404 deg/s^2 or 37.6% for all trials. Roll appears to have the lowest maximum RMSE for both techniques, followed by pitch and then yaw.
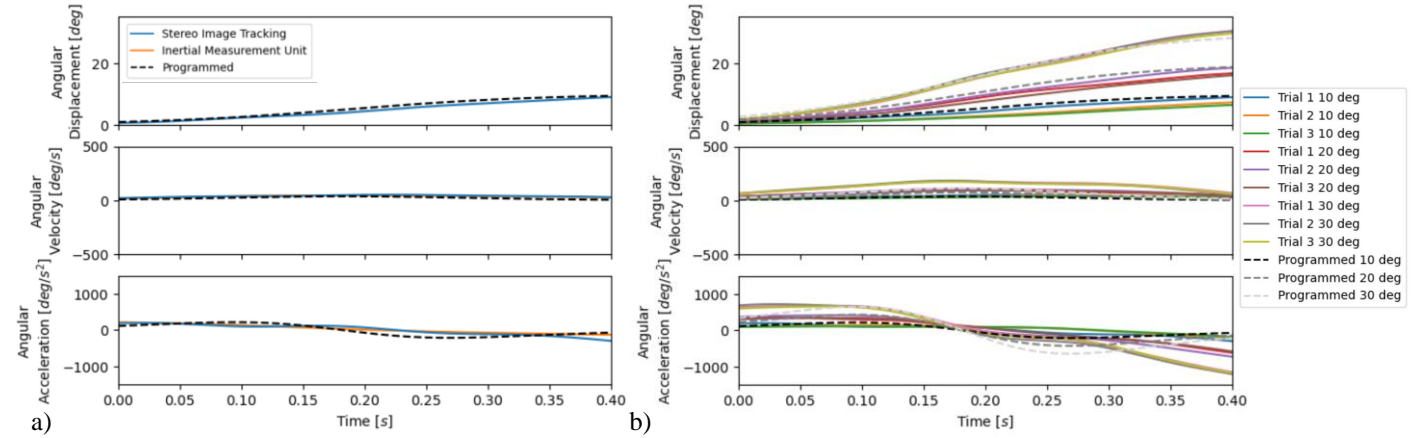

Fig. 13 a) Image tracking and IMU results overlaid on predicted motion for a typical trial and b) image tracking results overlaid on programmed motion for all trials of roll.
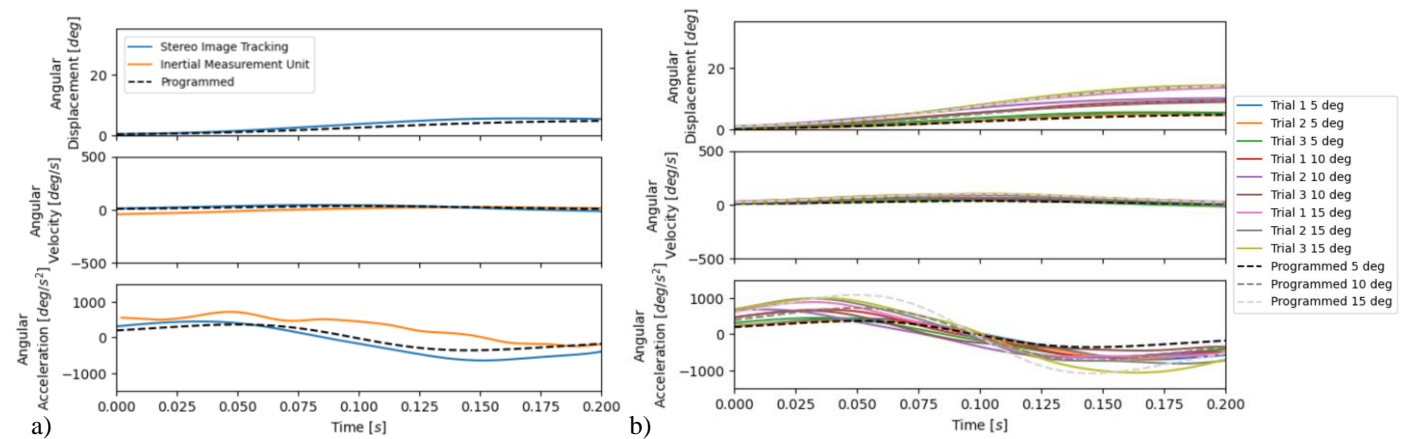

Fig. 14 a) Image tracking and IMU results overlaid on predicted motion for a typical trial and b) image tracking results overlaid on programmed motion for all trials of pitch.
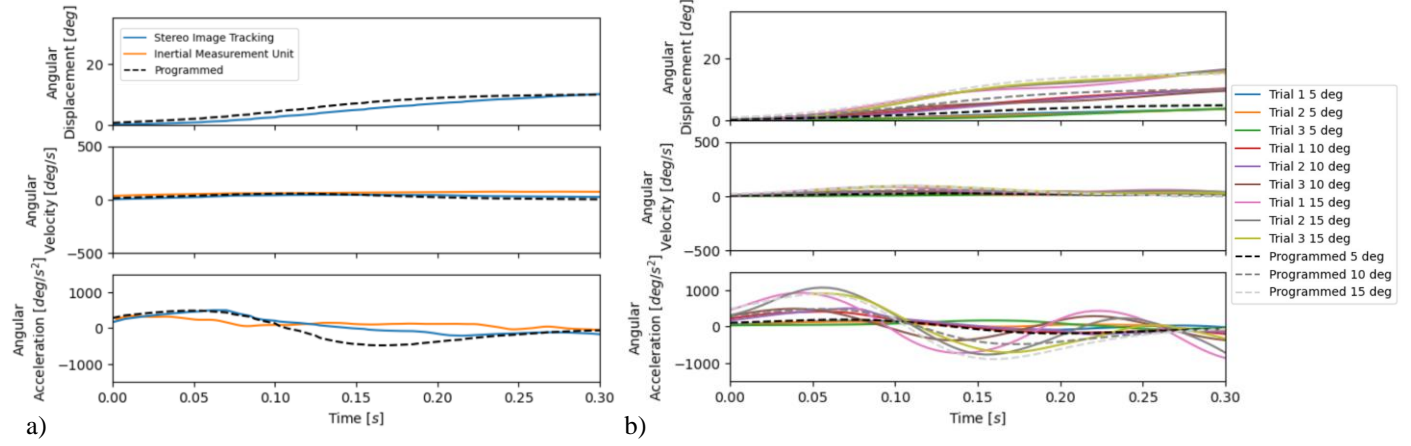
11

Fig. 15 a) Image tracking and IMU results overlaid on predicted motion for a typical trial and b) image tracking results overlaid on programmed motion for all trials of yaw.

Boxplots of the maximum differences between the two measurement techniques as well as the RMSE between each measurement technique and the programmed motion of the model for each of the nine trials about the x, y, and z axes are presented in Figures 16, 17, and 18 respectively. The ranges of the boxplots are tabulated in Table 5. For both the IMU and image tracking results, pitch and yaw have relatively large ranges of maximum RMSE and percentage RMSE compared to roll, perhaps indicating more reliable measurement of roll by both techniques.

Table 5   Ranges of maximum differences between measurement techniques and maximum RMSE for each technique

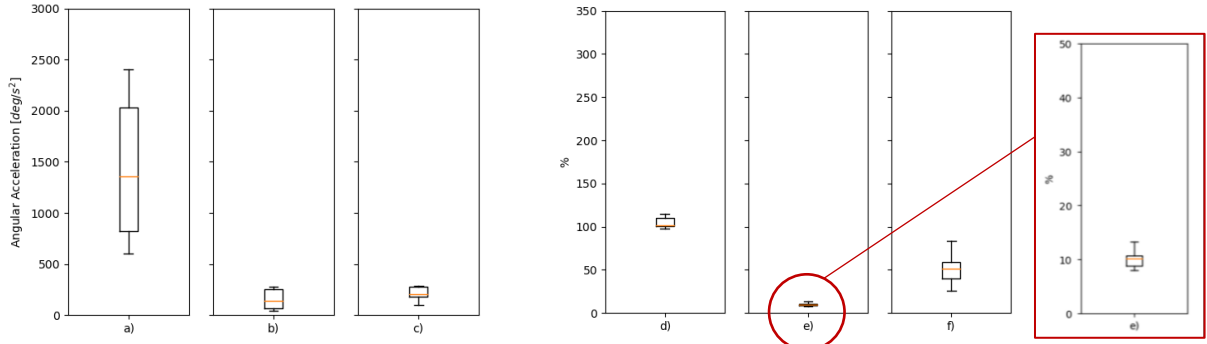| Axis	Range of $\Delta\alpha_{max}$ (deg/s²)	Range of %$\Delta\alpha_{max}$ (%)	Range of $RMSE_{max,IT}$ (deg/s²)	Range of %$RMSE_{max,IT}$ (%)	Range of $RMSE_{max,IMU}$ (deg/s²)	Range of %$RMSE_{max,IMU}$ (%)
X (Roll)	1800	16.2	236	5.26	189	57.8
Y (Pitch)	1960	101	191	31.5	606	289
Z (Yaw)	1100	89.4	375	25.5	539	91.9

Fig. 16 Boxplots of: a) $\Delta\alpha_{max}$, b) $RMSE_{max,IT}$, c) $RMSE_{max,IMU}$, d) %$\Delta\alpha_{max}$, e) %$RMSE_{max,IT}$ and e) %$RMSE_{max,IMU}$ for roll.
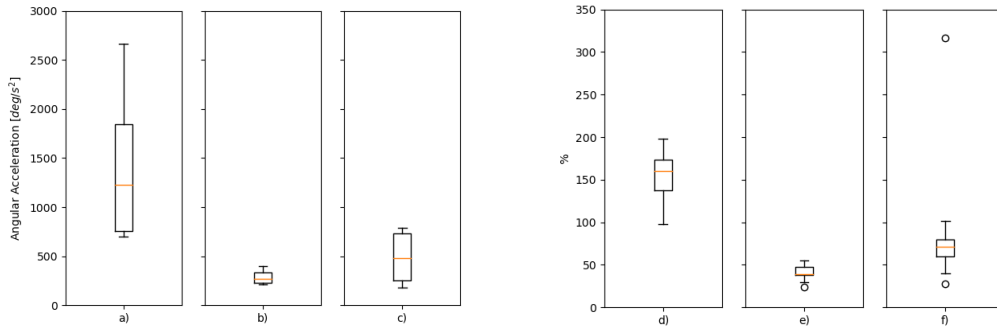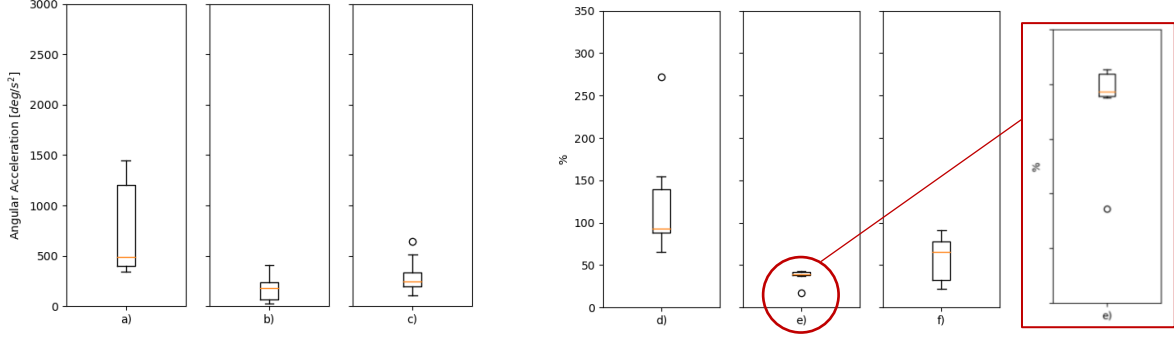

Fig. 17 Boxplots of: a) $\Delta\alpha_{max}$, b) $RMSE_{max,IT}$, c) $RMSE_{max,IMU}$, d) %$\Delta\alpha_{max}$, e) %$RMSE_{max,IT}$ and e) %$RMSE_{max,IMU}$ for pitch.

Fig. 18 Boxplots of: a) $\Delta\alpha_{max}$, b) $RMSE_{max,IT}$, c) $RMSE_{max,IMU}$, d) $\%\Delta\alpha_{max}$, e) $\%RMSE_{max,IT}$ and e) $\%RMSE_{max,IMU}$ for yaw.

C. Model Release

Displacement, velocity, and acceleration data from stereo image tracking and acceleration data from the onboard IMU are shown for each of the nine experiments. These results are then compared to the predicted motion of the freefalling model upon release from the wind tunnel release mechanism. Differences between the stereo image tracking and onboard IMU acceleration as well as and the RMSE between these data and the predicted motion are shown in Table 6.

Table 6   Maximum differences between measurement techniques and maximum RMSE for each technique

Δa_{max} (m/s^2)	a_{max} (m/s^2)	Predicted a (m/s^2)	$\%\Delta a_{max}$[1] (%)	$RMSE_{max,IT}$ (m/s^2)	$\%RMSE_{max,IT}$[2] (%)	$RMSE_{max,IMU}$ (m/s^2)	$\%RMSE_{max,IMU}$[3] (%)
0.919	10.7	9.81	8.57	0.617	5.72	0.0830	0.833

[1]Δa_{max} divided by the maximum acceleration (either $a_{max,IT}$ or $a_{max,IMU}$) measured in the trial containing Δa_{max}.
[2]$RMSE_{max,IT}$ divided by $a_{max,IT}$ in the trial containing $RMSE_{max,IT}$.
[3]$RMSE_{max,IMU}$ divided by $a_{max,IMU}$ in the trial containing $RMSE_{max,IMU}$.

Figure 19 shows both the stereo image tracking and onboard IMU results from the trial with the maximum difference between techniques overlaid on a plot of the predicted motion of the model and the stereo image tracking results from all nine trials along each axis overlaid on plots of the predicted motion of the model. Larger versions of these figures are shown in Appendix C. Relatively good agreement can be observed between the stereo image tracking results and the IMU results. In terms of the image tracking results, relatively good agreement can also be observed across these results across and indeed between these results and the predicted motion of the model, with RMSE remaining below 0.617 m/s^2 or 5.72% for all trials. The IMU results appear to have a far lower maximum RMSE of 0.0830 m/s^2 or 0.833%, indicating excellent agreement with the predicted motion of the model.
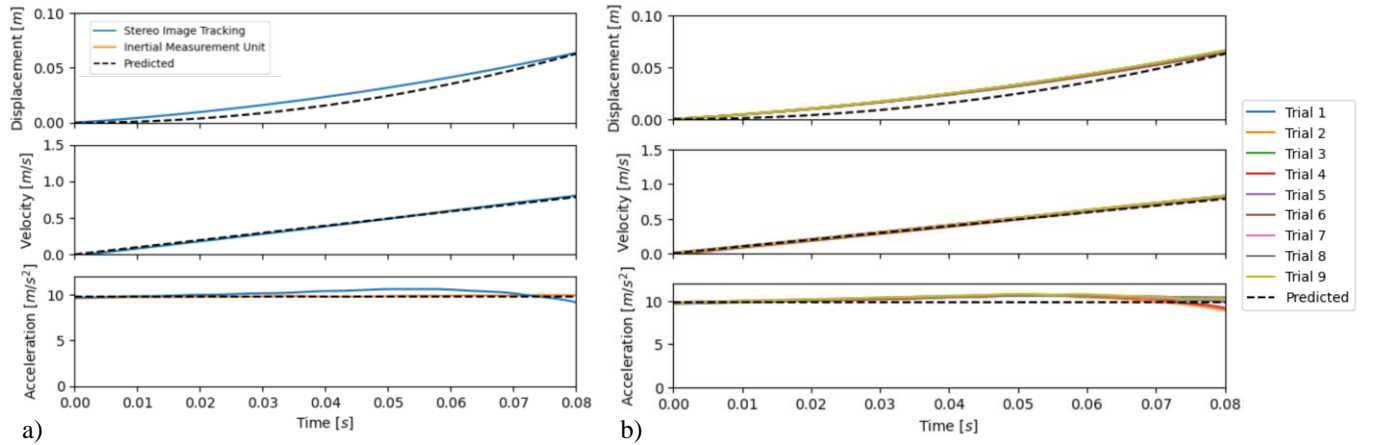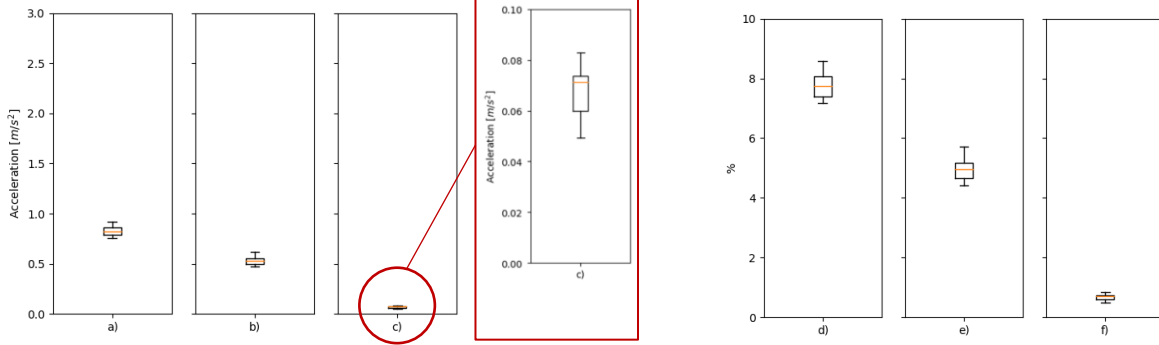

Fig. 19 a) Image tracking and IMU results overlaid on predicted motion for a typical trial and b) image tracking results overlaid on predicted motion for all trials of model release.

Boxplots of the maximum differences between the two measurement techniques as well as the RMSE between each measurement technique and the predicted motion of the model for each of the nine trials are presented in Figure 20. The ranges of the boxplots are tabulated in Table 7. There is a relatively low degree of variability in the maximum difference between the two techniques and in the maximum RMSE of the image tracking results and an even lower degree of variability in the maximum RMSE of the IMU results, indicating reliable measurement of accelerations by both techniques.

Table 7   **Ranges of maximum differences between measurement techniques and maximum RMSE for each technique**

Range of Δa_{max} (m/s^2)	Range of $\%\Delta a_{max}$ (%)	Range of $RMSE_{max,IT}$ (m/s^2)	Range of $\%RMSE_{max,IT}$ (%)	Range of $RMSE_{max,IMU}$ (m/s^2)	Range of $\%RMSE_{max,IMU}$ (%)
0.159	1.40	0.148	1.57	0.0338	0.337

Fig. 20 Boxplots of: a) %Δa$_{max}$, b) RMSE$_{max,IT}$, c) RMSE$_{max,IMU}$, d) %Δa$_{max}$, e) %RMSE$_{max,IT}$ and e) %RMSE$_{max,IMU}$ for release.

D. Summary of Results

Overall, image tracking had lower maximum RMSE, percentage RMSE, and ranges for both of these values than the IMU except in model release, indicating more accurate and reliable measurement by the stereo photogrammetry system in translation and rotation. The image tracking results had lower maximum RMSEs in translation compared to model release despite large differences in accelerations between them, however, lower measured accelerations in translation resulted in misleadingly higher percentage RMSEs for translation. Image tracking results for rotation had similar percentage RMSE to translation, except for a relatively high maximum value in yaw. On the other hand, the IMU had lower maximum percentage RMSE and ranges of maximum percentage RMSE for model release compared to translation and finally rotation. Maximum RMSE in the IMU results was lower for model release than for translation, despite large differences in measured accelerations, perhaps indicating improved performance and reliability of the IMU when measuring larger accelerations.

In terms of the maximum differences between techniques, these were similar for model release and translation, however, with far higher percentage values and ranges of these values for translation due to lower measured accelerations. Maximum percentage differences for rotation were similar to translation, as were the ranges of the maximum percentage differences, with lower percentage differences and ranges of percentage differences occurring for translation along and rotation about the x-axis. In the image tracking results for translation and rotation, the lowest maximum RMSE, maximum percentage RMSE and ranges for these values also occurred for the x-axis. This was also the case for the IMU results for rotation but not translation.

Linear regression of the IMU and image tracking results for each experiment was performed, however, no clear trends were observed. The maximum RMSEs for each trial were also examined and no obvious trends were observed, for example, an increase or decrease in maximum RMSE or maximum percentage RMSE with increasing or decreasing displacement or angular displacement.

E. Sources of Error

Error in the image tracking results for all 63 experiments could be due to numerous possible sources of error cited in the literature, including depth of field, exposure, marker positioning, lighting and contrast, optical distortion, motion-related blurring, pixelation, calibration errors, optical system misalignment, and noise amplification due to differentiation of displacement-time data in postprocessing [14,16-18,26-30,40]. Noise amplification due to differentiation in postprocessing, coupled with filtering to reduce noise, are particularly likely sources of error, and so will be discussed further in this section.

Examining the image tracking results for model release and translation, however, the maximum RMSEs when compared to the predicted or programmed motion of the model were 0.617 m/s^2 and 0.125 m/s^2 respectively, low enough to imply that the aforementioned sources would account for a relatively small degree of error across the 63 experiments. In Fig. 19, the deviation of the image tracking results from the IMU results and predicted motion of the model appear to be very similar across the nine experiments, perhaps indicating that the error due to these sources is systematic in nature. An alternative explanation for this could be some degree of motion imparted by the release mechanism upon model release, however, no such systematic error was identified in the IMU results and is therefore considered unlikely.

Examining the IMU results for translation, on the other hand, there is a significant level of noise in the results even after filtering, likely due to vibration of the translating stage with the stopping and starting behaviour of the stepper motor used to drive the stage. Spectral plots of the IMU data (Appendix D) showed peaks at multiples of 30 Hz from 30 to 240 Hz, caused by the interaction between the sampling rate of the IMU and the pulse rate of the stepper motor used to translate the stage. Considerably smaller peaks of the same frequencies were also noted in the spectral plots of the image tracking results, however, the maximum

RMSEs of these results remained well below the maximum RMSE for model release and so were largely unaffected after filtering. The IMU results were far noisier, however, with significantly larger maximum RMSEs compared to the IMU results for model release, likely due to the IMU being adhered to the model by means of double-sided tape, which may have allowed some movement of the IMU due to the constant stepping motion of the stage.

Given the lower degrees of maximum RMSE in both the image tracking and IMU results for rotation about the x-axis compared to the y- and z-axes, there are likely to be other sources of error in these results arising from either postprocessing or the mechanism used to rotate the model. In the case of image tracking results, possible sources of error include both errors in the positioning of the markers on the model and indeed in the positioning of the model on the mechanism to facilitate motion about its ideal COG. These would have more of an influence on pitch and yaw than on roll, as calculation of roll relies only on measured marker displacements and model radius, while calculation of pitch and yaw rely on measured marker displacements and the distance of the markers from the point about which the model rotates. Misalignment of the translating stage and rotating mechanism with the coordinate system by which displacements are measured by the stereo photogrammetry system was considered as a possible source of error in the image tracking results for translation and rotation. However, the maximum out-of-plane displacements of the model markers in the translation and rotation experiments were a mere 0.581 mm and 0.582 mm respectively.

In terms of the IMU results for rotation, possible sources of error include error in the positioning of the IMU within the model so as to measure angular velocities about the ideal COG, and erroneous triggering of the gyroscope, particularly for the yaw results which appear to differ significantly across the nine trials with no clear relationship between them. Possible sources of error for both measurement techniques include amplification of error in the calculation of angular displacements, and therefore angular velocities and angular accelerations as well as potential inability of the rotating mechanism to completely resist the higher rotational inertia of the model in pitch and yaw, and therefore follow the programmed motion with a high degree of fidelity.

Despite these sources of error, the results suggest a maximum RMSE of between 0.0755 and 0.617 m/s^2 for measurement of accelerations and of between 29.0 and 404 deg/s^2 for measurement of angular accelerations by the stereo photogrammetry system. In contrast, the results indicate a maximum RMSE of between 0.0492 and 0.686 m/s^2 for measurement of accelerations and of between 100 and 786 deg/s^2 for measurement of angular accelerations by the IMU. Since the possible range of maximum RMSE for the image tracking results would tend to provide a smaller RMSE than the possible range for the IMU, it would be appropriate to use the stereo photogrammetry system described herein to validate IMU measurements and could even be argued that the stereo photogrammetry system may prove to be a more reliable measurement technique. The potential of the stereo photogrammetry system to validate IMU measurements is further supported by the agreement observed between the two techniques in the translation and model release experiments, and indeed the more favourable performance of the stereo photogrammetry system when the model underwent vibration on the translating stage, which could prove advantageous in wind tunnel environments.

F. Recommendations for Future Work

The key limitations of the work described herein include a relatively small number of trials, motion being restricted to pure translation along or rotation about a particular axis in any one experiment, and experiments being performed on a benchtop rather than in a wind tunnel. Difficulties with vibration in the case of the translating stage and the inability of the rotating stage to resist the model's rotational inertia were also limitations in determining the level of fidelity with which these mechanisms facilitated the programmed motion.

Recommendations for future work include performing similar analysis to the work detailed herein for more complex 3-D motion, for example, known model trajectories facilitated by a robotic arm combining translation along and rotation about multiple axes. This would provide further insight into the capability of the system to measure 3-D motion in more realistic scenarios where motion is no longer constrained to a single axis or plane.

Testing of the stereo photogrammetry system in a hypersonic wind tunnel facility is also recommended to enable more detailed investigation into sources of error unique to wind tunnel environments like tunnel vibration and image distortion by the tunnel windows. Finally, comparison of the accuracy, reliability, and ease of use of the stereo photogrammetry system with other approaches like the use of Bayesian state estimation by Lock et al. [40] is recommended to identify whether further development of the approach described herein would be worthwhile.

VI. Conclusion

The primary objective of this work was to develop and test a new stereo photogrammetry system for multi-axis optical tracking of free-flight models. The system employed two synchronized high-speed cameras mounted at 45 degrees from the horizontal on either side of a simulated test section and was successfully used to track pure translation along and rotation about all three axes of motion, in addition to model release. The secondary objectives of this work were to characterise the uncertainty in the measurements taken with this system and to demonstrate its successful validation of IMU results in the case of model release. Uncertainties were characterised in terms of the maximum RMSEs between image tracking results and the predicted motion of the model and remained below 0.617 m/s^2 and 404 deg/s^2 for acceleration and angular acceleration results respectively. The system was then successfully used to validate IMU acceleration results in the case of model release, with a maximum difference of 0.159 m/s^2 between the IMU and image tracking acceleration results. Errors were largely attributed to systematic errors in the stereo photogrammetry system, noise amplification due to differentiation in postprocessing, and issues with the translating stage, rotating mechanism, and triggering of the IMU. Further testing of the system's ability to track complex 3-D motion combining translations along and rotations about multiple axes is recommended, as is testing of the system in a hypersonic wind tunnel facility, to further investigate its capability for accurate and reliable measurement of aerodynamic forces.

Acknowledgments

References

[1] Anderson, J. D., *Hypersonic and High Temperature Gas Dynamics*, 1st ed., McGraw–Hill, New York, 1989.

[2] Kennell, C., Neely, A., O'Byrne, S., and Buttsworth, D., "Measurement of Vehicle Stability Coefficients in Hypersonic Wind Tunnels," *20th AIAA International Space Planes and Hypersonic Systems and Technologies Conference*, AIAA, Glasgow, Scotland, 2015, p. 3690.

[3] McQuellin, L. P., Kennell, C. M., Neely, A. J., Sytsma, M. J., Silvester, T., Choudhury, R. and Buttsworth, D. R., "Investigating Endo-Atmospheric Separation of a Hypersonic Flyer-Sustainer using Wind Tunnel based Free-Flight," *23rd AIAA International Space Planes and Hypersonic Systems and Technologies Conference*, AIAA, Montreal, Quebec, 2020, pp. 1-24.

[4] Mudford, N. R., O'Byrne, S., Balage, S., and Neely, A. J., "Hypersonic Wind Tunnel Free Flying Experiments with Onboard Instrumentation," *AIAA Journal of Spacecraft and Rockets*, Vol. 52, No. 1, 2014.

[5] Hyslop, A., Goherty, L. J., McGilvray, M., Neely, A., McQuellin, L. P., Barth, J. and Mullen, G., "Free-Flight Aerodynamic Testing of the Skylon Space Plane," *Journal of Spacecraft and Rockets*, Vol. 58, No. 5, 2021, pp. 1487–1497.

[6] Kennell, C., Neely, A. J., Buttsworth, D. R., Choudhury, R., and Tahtali, M., "Free Flight Testing in Hypersonic Flows: HEXAFLY-INT EFTV," *54th AIAA Aerospace Sciences Meeting*, AIAA, San Diego, CA, 2016, p. 1152.

[7] Sahoo, N., Suryavamshi, K., Reddy, K., and Mee, D., "Dynamic Force Balances for Short-Duration Hypersonic Testing Facilities," *Experiments in Fluids*, Vol. 38, No. 5, 2005, pp. 606–614.
https://doi.org/10.1007/s00348-005-0932-5

[8] Tanno, H., Komuro, T., Sato, K., and Itoh, K., "Free-Flight Force Measurement Technique in the Impulsive Facility HIEST," *22nd International Congress on Instrumentation in Aerospace Simulation Facilities*, IEEE, Pacific Grove, CA, 2007, pp. 1–5.

[9] Juhany, K. A., and Darji, A., "Force Measurement in a Ludwieg Tube Tunnel," *Journal of Spacecraft and Rockets*, Vol. 44, No. 1, 2007, pp. 88–93.

[10] Neely, A. J., West, I., Hruschka, R., Park, G. & Mudford, N. R. "Determining aerodynamic coefficients from high speed video of a free-flying model in a shock tunnel," *International Congress on High-Speed Imaging and Photonics*, Canberra, Australia, 2008.

[11] Lewis, H. and East, R., "Measurement of Free-Flight Dynamic Stability Derivatives of Cones in a Hypersonic Gun Tunnel," *AIAA Sixth International Aerospace Planes and Hypersonics Technologies Conference*, AIAA Paper-95-6082, Chattanooga, Tennessee, 1995.

[12] Tanno, H., Tomoyuki, K., Kazuo, S., Katsuhiro, I., and Masahiro, T., "Miniature Data Logger for Aerodynamic Force Measurement in Impulsive Facility," *27th AIAA Aerodynamic Measurement Technology and Ground Testing Conference*, AIAA Paper 2010-4204, 2010.

[13] Tanno, H., Komuro, T., Sato, K., Itoh, K., Takahashi, M., Fujita, K., Laurence, S., and Hannemann, K., "Free-Flight Force Measurement Technique in Shock Tunnel," *50th AIAA Aerospace Sciences Meeting*, AIAA Paper 2012-1241, Nashville, Tennessee, 2012.

[14] Laurence, S. J., and Karl, S., "Improved Visualization-Based Force Measurement Technique for Short-Duration Hypersonic Facilities," *Experiments in Fluids*, Vol. 48, No. 6, 2010, pp. 949–965.

[15] Laurence, S. J., and Hornung, H. G., "Image-Based Force and Moment Measurement in Hypersonic Facilities," *Experiments in Fluids*, Vol. 46, No. 2, 2009, pp. 343–353.
https://doi.org/10.1007/s00348-008-0565-6

[16] Seltner, P. M., Willems, S., and Gülhan, A., "Aerodynamic Coefficients of Free-Flying Cubes in Hypersonic Flowfield," *Journal of Spacecraft and Rockets*, Vol. 56, No. 6, 2019, pp. 1725–1734.

[17] Hyslop, A. M., McGilvray, M., and Doherty, L. J., "Free-Flight Aerodynamic Testing of a 7 Degree Half-Angle Cone," *AIAA SciTech 2022 Forum*, AIAA, Reston, Virginia, 2022.
https://doi.org/10.2514/6. 2022-1324

[18] Kennell, C., Reimann, B., Choudhury, R., Buttsworth, D., and Neely, A., "Subscale hypersonic free flight dynamics of HEXAFLY-INT EFTV+ESM (multibody separation)," *7th European Conference for Aeronautics and Space Science*, EUCASS, Bari, Italy, 2017.

[19] Tanno, H., Komuro, T., Sato, K., and Katsuhiro, I., "Aerodynamic characteristics of generic test models under high-temperature real-gas condition in free-piston shock tunnel HIEST," *15th AIAA International Space Planes and Hypersonic Systems and Technologies Conference*, AIAA, Dayton, Ohio, 2008.

[20] Tanno, H., Komuro, T., Sato, K., and Itoh, K., "Free-flight aerodynamic test of elliptic cone in Shock Tunnel," *20th AIAA International Space Planes and Hypersonic Systems and Technologies Conference*, AIAA, Glasgow, Scotland, 2015.
https://doi.org/10.2514/6.2015-3655

[21] Laurence, S. J., Parziale, N. J., and Deiterding, R., "Dynamical separation of spherical bodies in supersonic flow," *Journal of Fluid Mechanics*, Vol. 713, 2012, pp. 159–182.

[22] Reimann, B., Kennell, C., and Neely, A., "Simulation of Hypersonic Free-Flight Dynamics and Support Module Separation of the HEXAFLY-INT Glider," *68th International Astronautical* Congress, IAC, Adelaide, Australia, 2017.

[23] Pick, G. S., "Sting Effects in Hypersonic Base Pressure Measurements," Naval Ship Research and Development Center, TR AL-85, Bethesda, MD, December 1971.

[24] Owen, A. K. and Owen, F. K., "Hypersonic Free Flight Measurement Techniques," *22nd International Congress on Instrumentation in Aerospace Simulation Facilities*, IEEE, Pacific Grovem, CA, 2007, pp. 1-11.

[25] Laurence, S. J., Dieterding, R., and Hornung, H. G., "Proximal Bodies in Hypersonic Flow," *Journal of Fluid Mechanics*, Vol. 590, Nov. 2007, pp. 209–237.

[26] Shortis, M. R., and Snow, W. L., "Videometric Tracking of Wind Tunnel Aerospace Models at NASA Langley Research Center," *The Photogrammetric Record*, Vol. 15, No. 89, 2003, pp. 673-689.

[27] Gui, L., Murray, N. E., and Seiner, J. M., "Tracking an aerodynamic model in a wind tunnel with a stereo high-speed imaging system," *2010 3rd International Congress on Image and Signal Processing*, Yantai, China, 2010, pp. 1533-1537. https://doi.org/10.1109/CISP.2010.5647179

[28] Schairer, E. T., Kushner, L., Drain, B. A., Heineck, J. T., and Durston, D. A., "Stereo Photogrammetry Measurements of the Position and Attitude of a Nozzle-plume/Shock-wave Interaction Model in the NASA Ames 9- by 7- Ft Supersonic Wind Tunnel," *55th Aerospace Sciences Meeting*, AIAA, Grapevine, Texas, 2017.

[29] Kushner, L. K., Drain, B. A., Shairer, E. T., Heineck, J. T., and Bell, J. H., "Model Deformation and Optical Angle of Attack Measurement System in the NASA Unitary Plan Wind Tunnel," *55th Aerospace Sciences Meeting*, AIAA, Grapevine, Texas, 2017. https://doi.org/10.2514/6.2017-1052

[30] Zhang, M., Liang, J., Chen, L., Tang, Z., and Zong, Y., "A stereo photogrammetry system for model position and attitude measurement in hypersonic wind tunnel testing," *Review of Scientific Instruments*, Vol. 92, No. 7, 2021. https://doi.org/10.1063/5.0059161

[31] Moran, J. H., McQuellin, L. P., Pollock, L., and Neely, A. J., "Wind-Tunnel based Free-Flight Testing of a Viscous Optimised Hypersonic Waverider," *AIAA SciTech 2023 Forum*, AIAA, National Harbor, Maryland, 2023.

[32] Mee, D., Daniel, W., and Simmons, J., "Three-Component Force Balance for Flows of Millisecond Duration," *AIAA Journal*, Vol. 34, No. 3, 1996, pp. 590–595. https://doi.org/10.2514/3.1310

[33] Kemp, J. H., "Telemetry Measurements of Afterbody Pressures on Free-Flying Models of the Apollo Capsule at Mach Numbers from 10 to 21 in Helium and 14 in Air," NASA TM-X-1154, January 1965.

[34] McQuellin, L. P., Neely, A. J., and Currao, G. M. D., "Considerations for a Hypersonic Flight Test Investigating Fluid-Thermal-Structural Interactions," *23rd AIAA International Space Planes and Hypersonic Systems and Technologies Conference*, AIAA, Montreal, Canada, 2020.

[35] Grant, B., Stone, H., Withers, P., and Preuss, M., "High-temperature strain field measurement using digital image correlation," *The Journal of Strain Analysis for Engineering Design*, Vol. 44, No. 4, 2009, pp. 263–271.

[36] Culler, A., Williams, T., and Bolender, M., "Aerothermal modeling and dynamic analysis of a hypersonic vehicle," *AIAA Atmospheric Flight Mechanics Conference and Exhibit*, AIAA, Keystone, CO, 2007, p. 6395

[37] Steelant J., "ATLLAS: Aero-Thermal Loaded Material Investigations for High-Speed Vehicles", *15th AIAA International Space Planes and Hypersonic Systems and Technologies Conference*, AIAA, Dayton, Ohio, 2008.

[38] Intrieri, P. F., and Kirk, D. B., "High-Speed Aerodynamics of Several Blunt-Cone Configurations," *Journal of Spacecraft and Rockets*, Vol. 24, No. 2, 1987, pp. 127–132. https://doi.org/10.2514/3.25885

[39] Meyn, L. A., and Bennett, M. S., "Application of a Two Camera Video Imaging System to Three-Dimensional Vortex Tracking in the 80- by 120-Foot Wind Tunnel," AIAA, AIAA Paper 93-3439, January 1993.

[40] Lock, A., Armstrong, G., Hack, F., Birch, B., Buttsworth, D., and Jahn, I., "Optical aerodynamic measurements of hypersonic free-flight using Bayesian state estimation," *AIAA Aviation 2023 Forum*, AIAA, San Diego, California, 2023. https://doi.org/10.2514/6.2023-371

[41] Birch, B., Buttsworth, D., and Zander, F., "Laser-Induced Diaphragm Rupture Method for Free Flight Experiments in a Hypersonic Ludwieg Tube Facility," *Journal of Spacecraft and Rockets*, Vol. 60, No. 4, 2022, pp. 1-10. https://doi.org/10.2514/1.A35427

[42] Chong, A. K., Buttsworth, D., Mudford, N., Jokic, M., Balage, S. and O'Byrne, S., "Application of photogrammetry at USQ hypersonic wind tunnel," *11th Australian Space Science Conference (ASSC 2011)*, ASSC, Canberra, Australia, 2011.
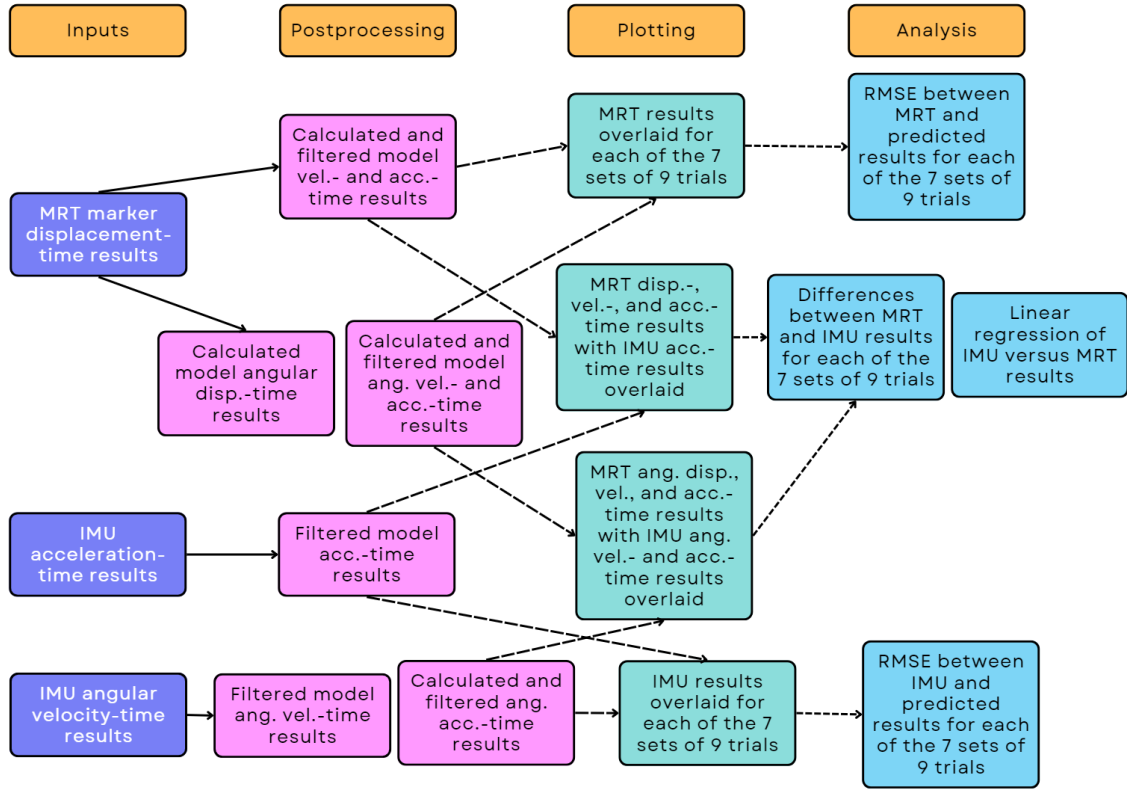
Fig. 1   Diagrammatic representation of custom Python code used for postprocessing.

Appendix B.   Uncertainty Calculations

Calculation of velocities and accelerations from the image tracking results and of angular accelerations from the IMU results relies on differentiation of displacement and angular velocity data respectively. Differentiation is performed by subtracting each pair of two adjacent values in a time series and dividing them by the timestep between measurements according to the equation:

$$v_i = \frac{x_i - x_{i-1}}{dt} \quad (B1)$$

Typical uncertainty calculations would see the uncertainty in each resultant value calculated by adding the absolute uncertainties in the values undergoing subtraction and dividing by the timestep between measurements according to the equation:

$$U_{v_i} = \frac{U_{x_i} + U_{x_{i-1}}}{dt} \quad (B2)$$

The timestep used in these calculations is determined by the sampling rate of the stereo photogrammetry system or IMU.

In the case of angular displacements calculated from the image tracking results, the Taylor series method is used to determine the propagation of uncertainties in calculating these values using the cosine rule:

$$\theta = \cos^{-1}\left(\frac{2r^2 - x^2}{2r^2}\right)(B3)$$

Displacement in this case is the overall displacement of the markers in the plane in which the model rotates, while the radius is the radius of the model in the case of roll or the distance between the particular marker for which angular displacement is being calculated and the model's COG for pitch and yaw. Uncertainties in angular displacement are therefore calculated using the equation:

$$U_\theta = \sqrt{(\frac{\partial\theta}{\partial r})^2 \times U_r + (\frac{\partial\theta}{\partial x})^2 \times U_x} \ (B4)$$

This equation relies on knowledge of the absolute uncertainties in marker displacement (0.1 mm from Table 1), model radius (0.5 mm), and distance between each marker and the model's COG (0.5 mm). Angular velocities and angular accelerations are then calculated using equation (B1) and their absolute uncertainties are calculated using equation (B2).

Overall, use of these equations sees absolute uncertainties quoted in terms of the values presented in Table 1. These values are extremely large for frame rates above 200 fps and provide a poor indication of the capability of the stereo photogrammetry system and indeed the IMU to provide meaningful results. For example, the uncertainty in image tracking acceleration results quoted for the model release experiments with a frame rate of 1000 fps would require a minimum acceleration of 400 m/s² before the system could be certain the model was accelerating rather than decelerating.

Table 1   Uncertainties in measured and programmed values.

	Sampling Rate (Hz)	Displacement (m)	Velocity (m/s)	Acceleration (m/s^2)	Angular Displacement (deg)	Angular Velocity (deg/s)	Angular Acceleration (deg/s^2)
Programmed Motion for Translating Stage	100	0.0004[1]	0.08	16			
Programmed Motion for Rotating Mechanism	200 500				0.5[2]	200 500	80 000 500 000
Stereo photogrammetry system	100	0.0001[3]	0.02	4	0.6	120	24 000
	200		0.04	16		240	96 000
	500		0.1	100		600	600 000
	1000		0.2	400		1200	2 400 000
IMU	100			3[4]		30[5]	6 000
	200						12 000
	500						30 000
	1000						60 000

[1]Determined by taking repeated measurements of programmed displacements with a digital calliper.
[2]Determined by taking repeated measurements of programmed angular displacements with a protractor.
[3]Maximum displacement obtained from tracking the displacement of a stationary model; agrees with previous work in TUSQ by Chong et al. [42].
[4]Maximum acceleration obtained from measuring the acceleration of a stationary model.
[5]Maximum angular velocity obtained from measuring the angular velocity of a stationary model.

In hypersonic wind tunnel facilities with flow durations of only one to a few hundred milliseconds, higher frame rates upward of 1000 fps are often required to obtain a sufficient number of data points from the experiments being conducted. Even in the case

of 500 fps, the uncertainties quoted for angular acceleration in yaw would require angular accelerations upward of 30 000 deg/s before the IMU could determine the sign of the angular acceleration results with certainty.

The standard method of uncertainty propagation also fails to account for filtering of the results, particularly between differentiations to reduce amplification of noise in further differentiation. Filtering is common in the literature [2,4-6,16,17,21] and is often necessary to make sense of the IMU and image tracking results as even the propagation of uncertainty in differentiation demonstrates the significant extent to which noise can be amplified when dividing by relatively short timesteps.

Instead of relying on the standard method, this work seeks to characterise the accuracy of the stereo photogrammetry system by comparing the results obtained from image tracking to the programmed or predicted motion of the model and indeed to the results obtained by the IMU. RMSE between the image tracking results and the programmed or predicted motion of the model and indeed between the IMU results and the programmed or predicted motion of the model are used as an indicator of measurement error which also accounts for the noise reduction performed in postprocessing. The range of maximum RMSEs from each group of nine trials also aids in assessment of the reliability of the IMU and stereo photogrammetry system.
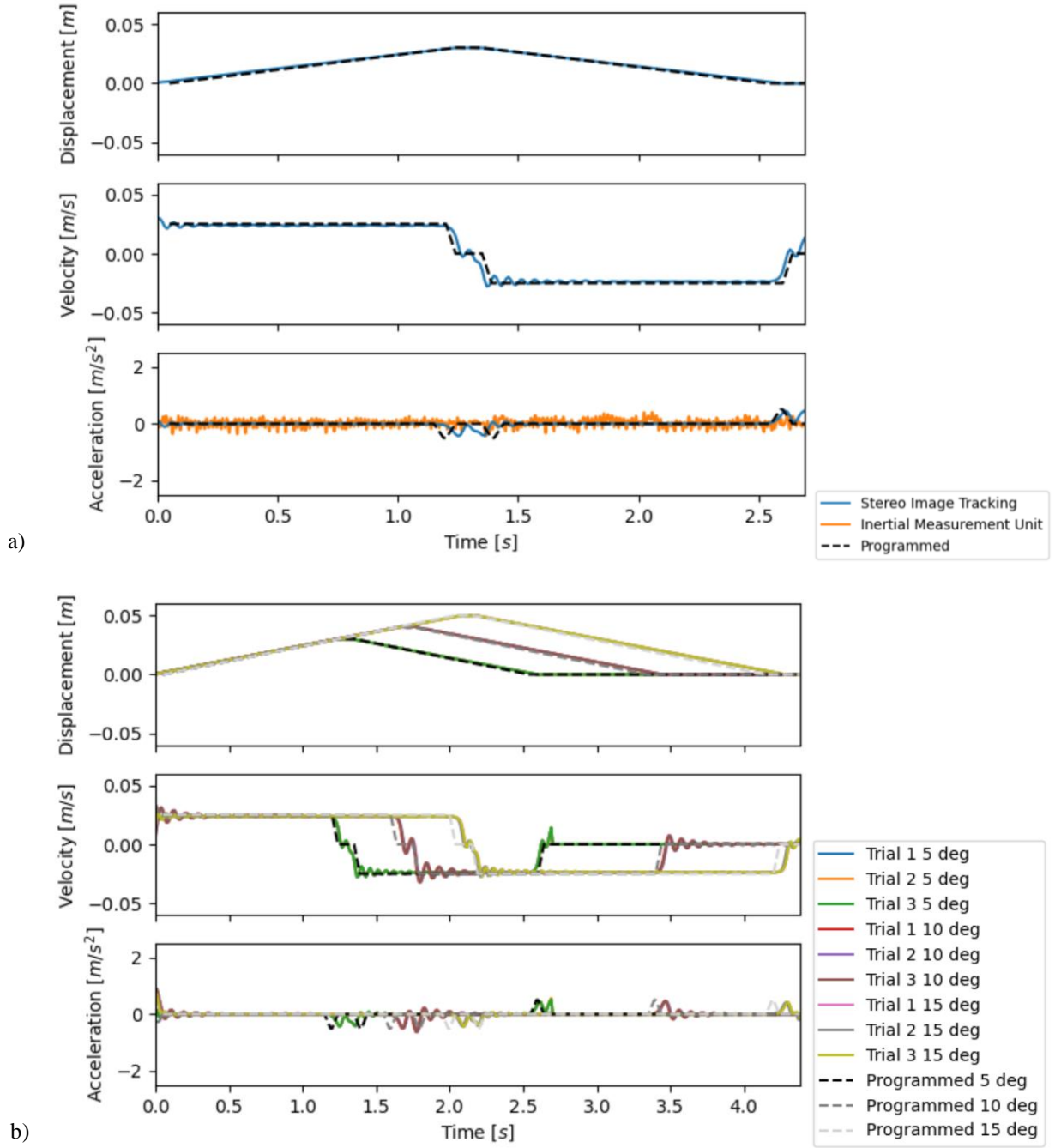
a)

b)

Fig. 1   a) Image tracking and IMU results overlaid on predicted motion for a typical trial and b) image tracking results overlaid on programmed motion for all trials of translation along the x-axis.
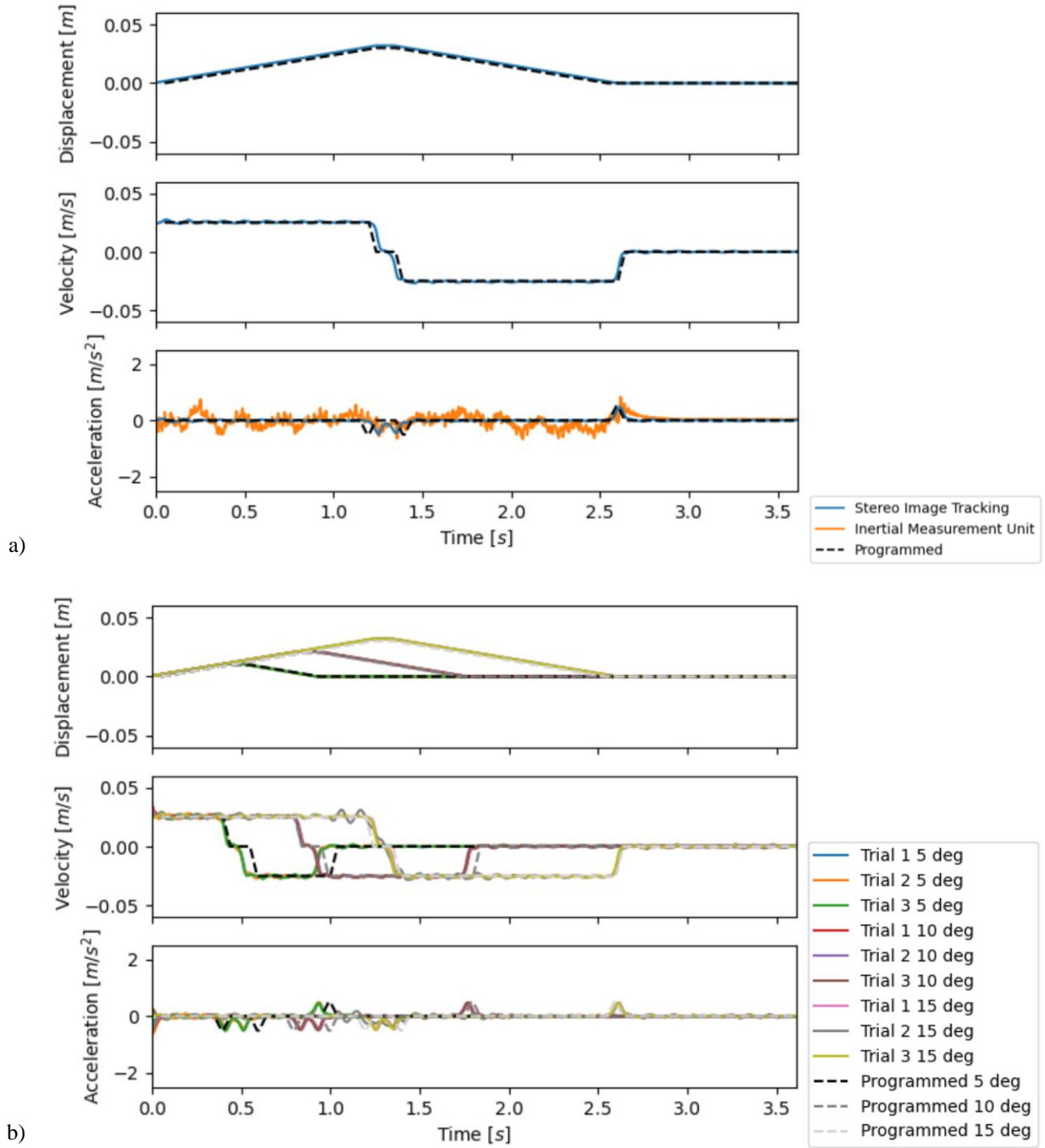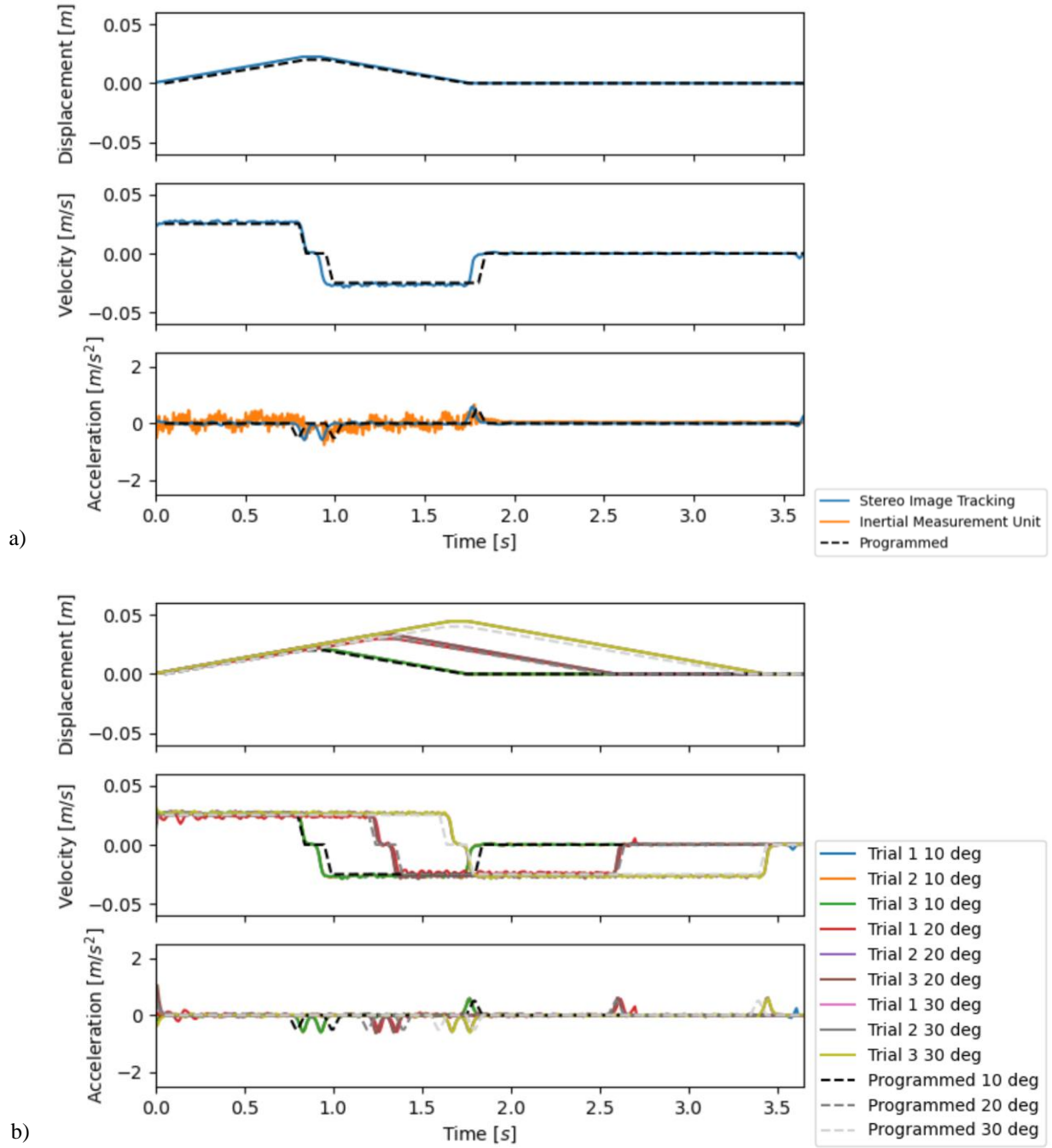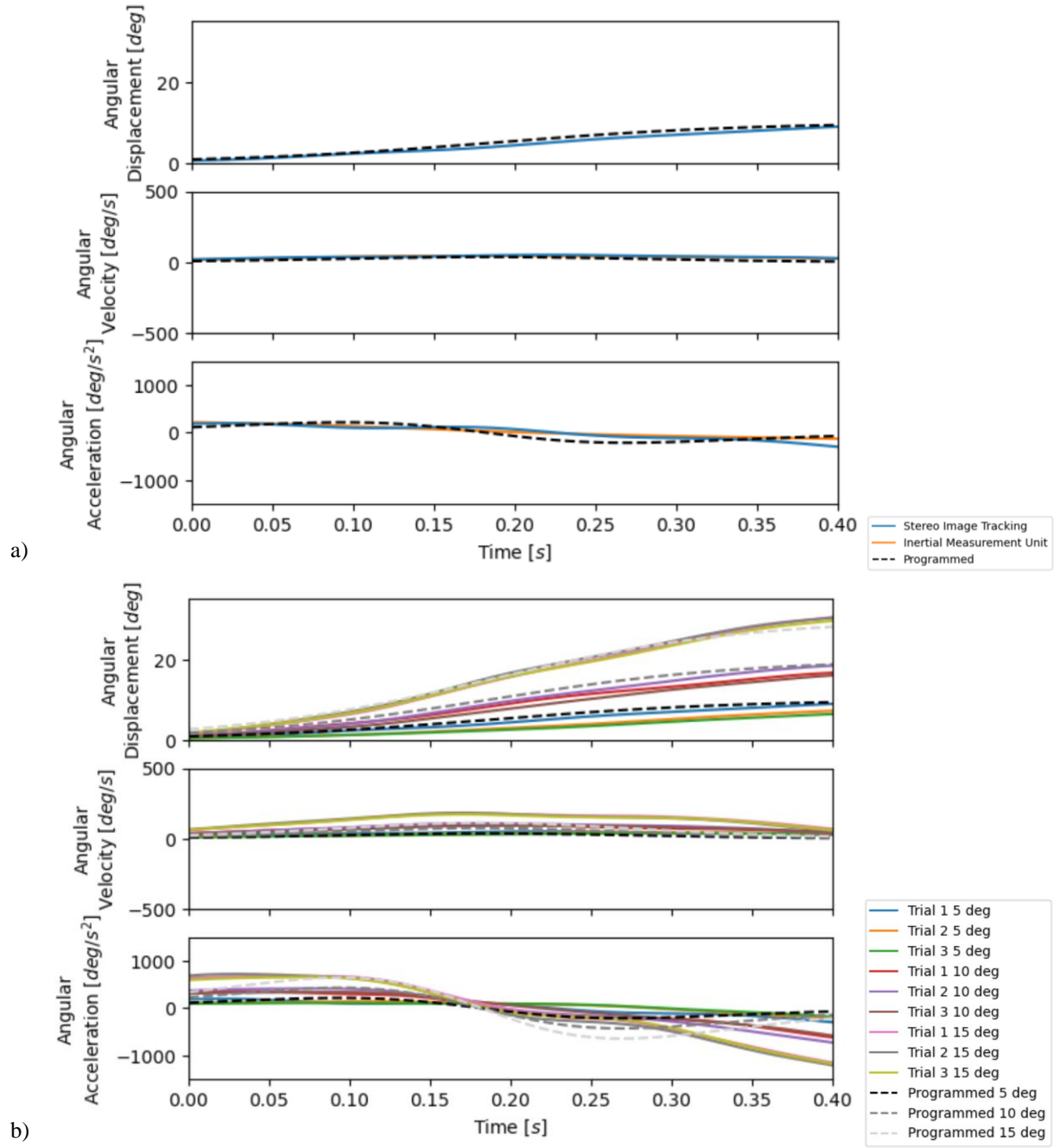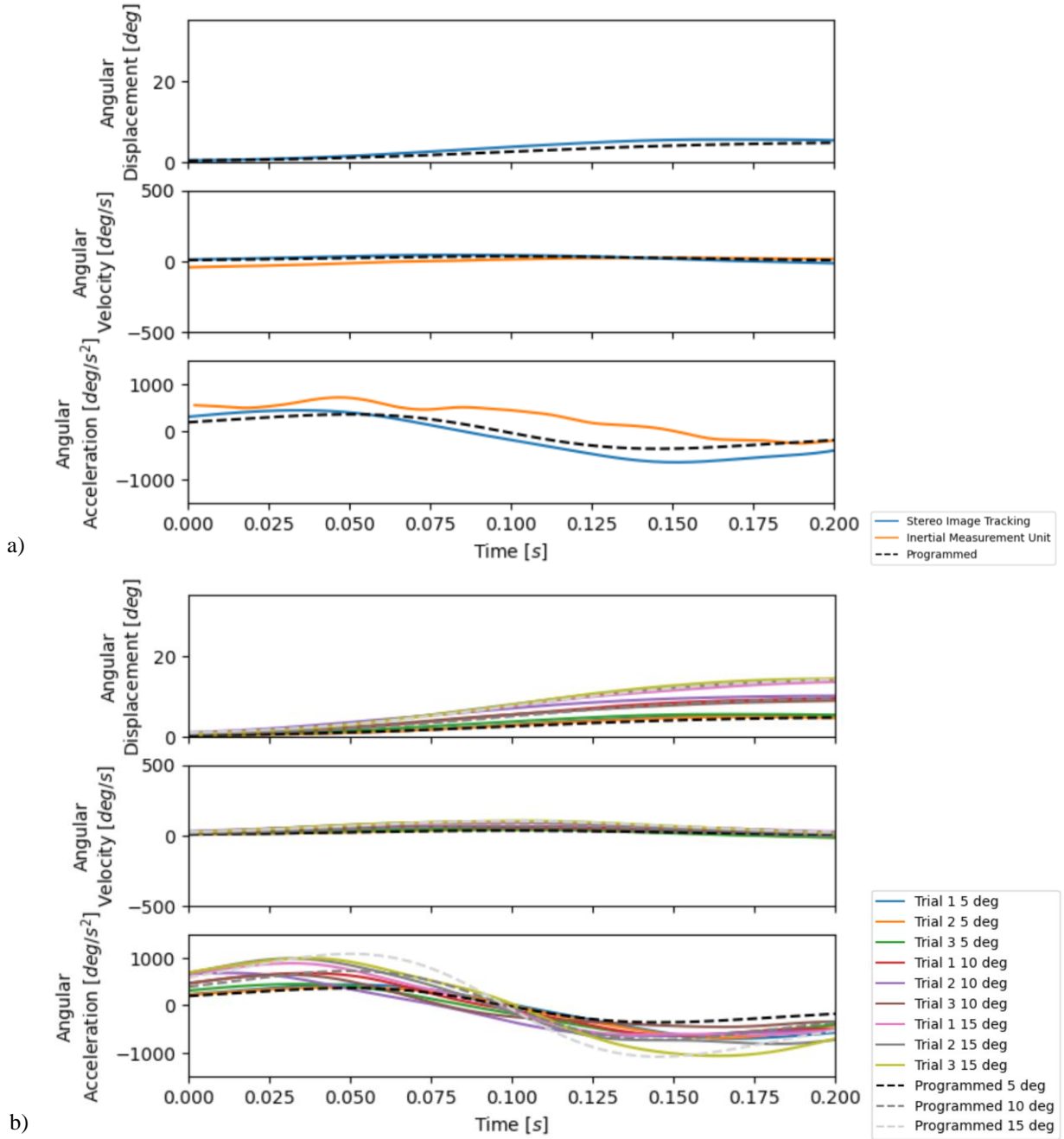
Fig. 2 a) Image tracking and IMU results overlaid on predicted motion for a typical trial and b) image tracking results overlaid on programmed motion for all trials of translation along the y-axis.

Fig. 3 **a) Image tracking and IMU results overlaid on predicted motion for a typical trial and b) image tracking results overlaid on programmed motion for all trials of translation along the z-axis.**

Fig. 4 a) **Image tracking and IMU results overlaid on predicted motion for a typical trial and b) image tracking results overlaid on programmed motion for all trials of roll.**
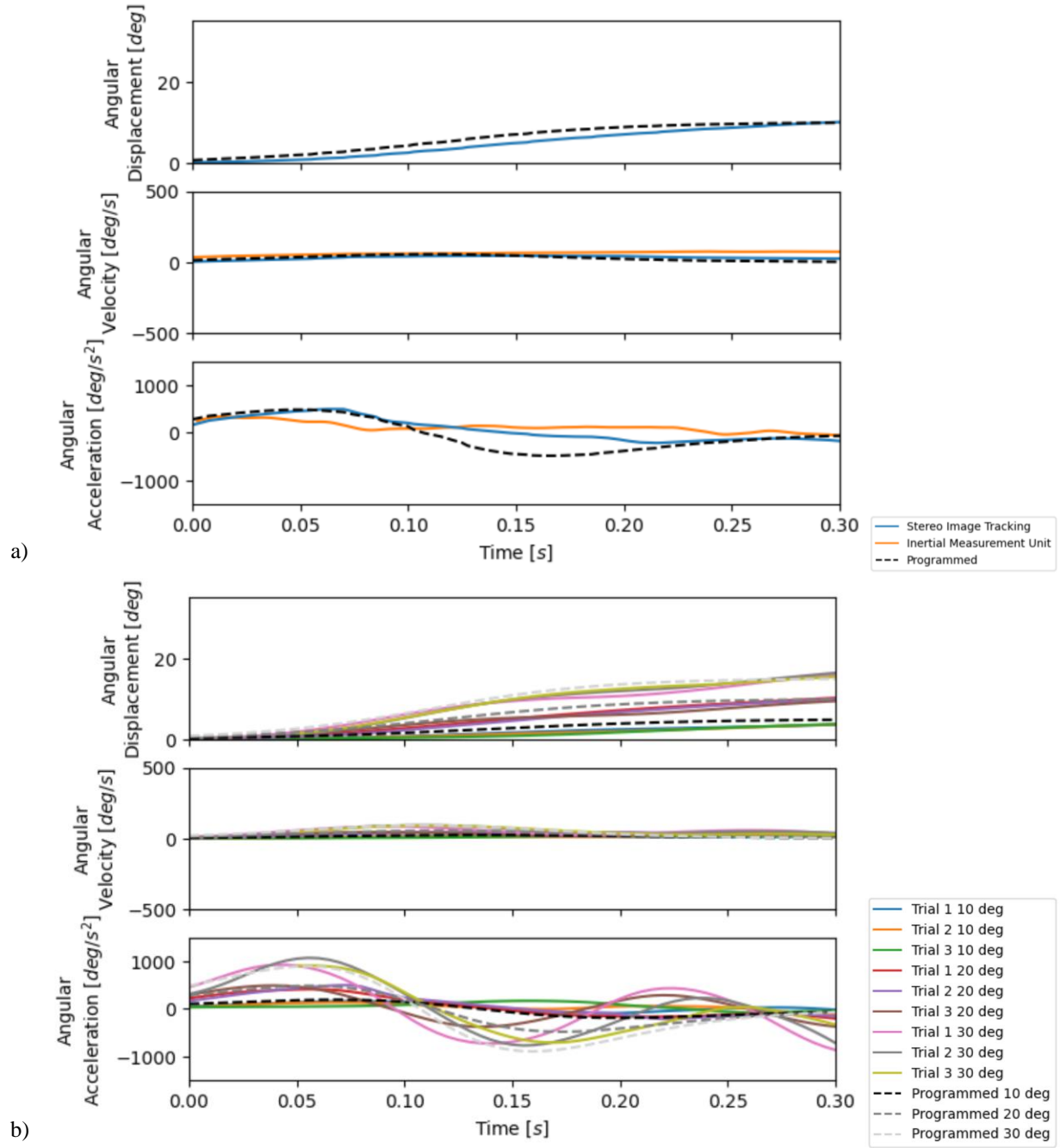
Fig. 5   a) Image tracking and IMU results overlaid on predicted motion for a typical trial and b) image tracking results overlaid on programmed motion for all trials of pitch.

Fig. 6 a) Image tracking and IMU results overlaid on predicted motion for a typical trial and b) image tracking results overlaid on programmed motion for all trials of yaw.
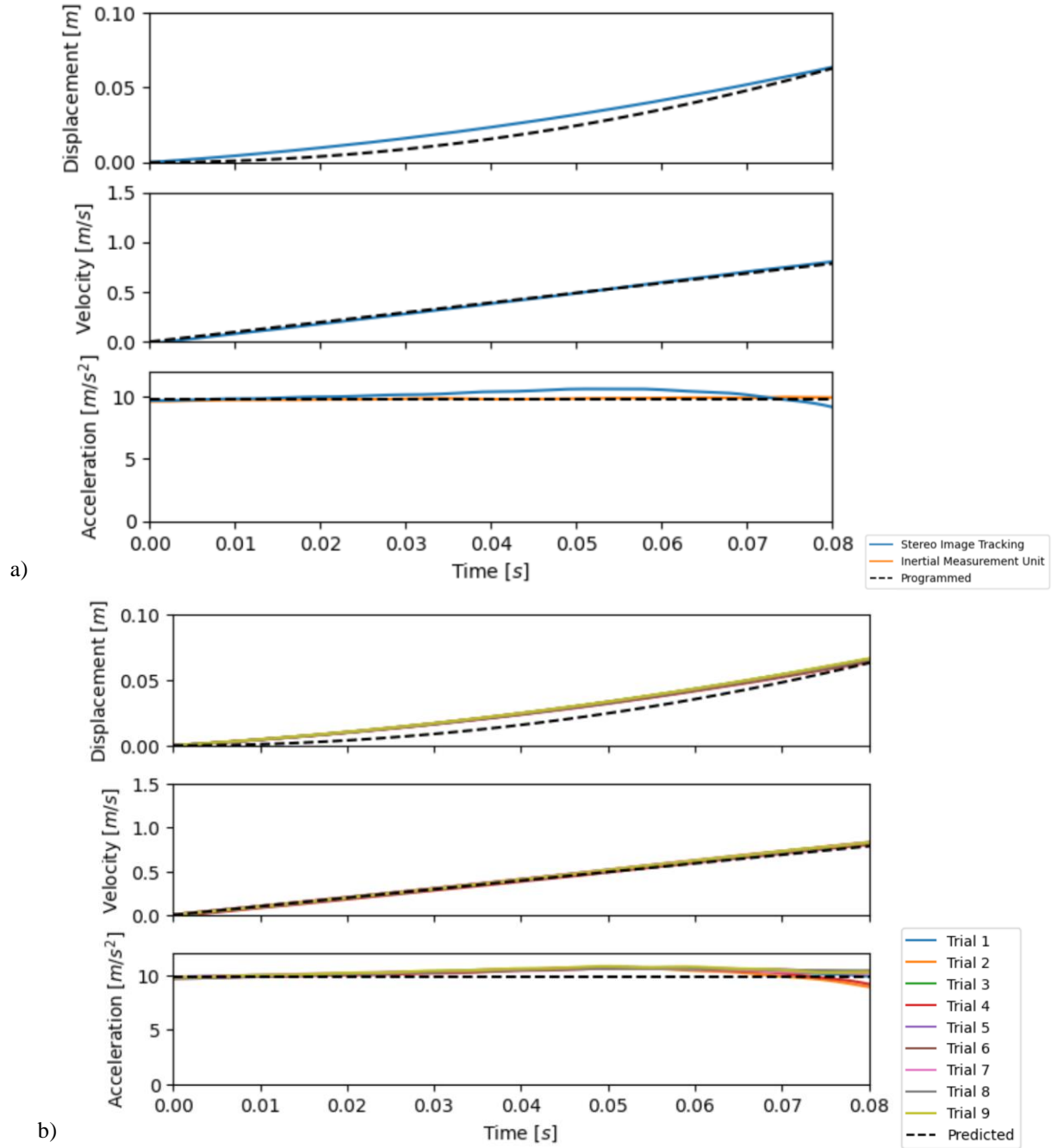
Fig. 7   a) Image tracking and IMU results overlaid on predicted motion for a typical trial and b) image tracking results overlaid on predicted motion for all trials of model release.

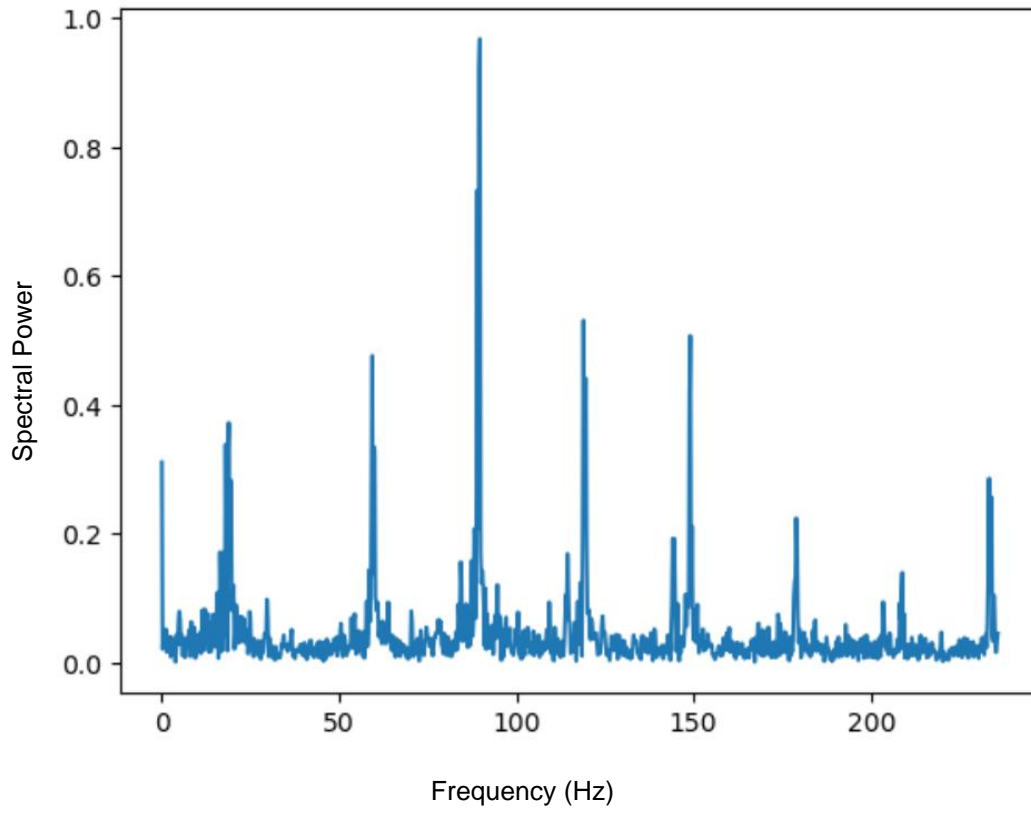**Appendix D.   Spectral Plot of IMU Results for Translation**

Fig. 1   Typical spectral plot of IMU results for translation.